Redox Biology 37 (2020) 101703

Contents lists available at ScienceDirect

Redox Biology

journal homepage: www.elsevier.com/locate/redox

Research Paper

AIBP protects retinal ganglion cells against neuroinflammation and mitochondrial dysfunction in glaucomatous neurodegeneration

Soo-Ho Choi [a,1,**], Keun-Young Kim [b,1], Guy A. Perkins [b], Sébastien Phan [b], Genea Edwards [c,2], Yining Xia [a], Jungsu Kim [a], Dorota Skowronska-Krawczyk [d], Robert N. Weinreb [c], Mark H. Ellisman [b], Yury I. Miller [a,3], Won-Kyu Ju [c,1,*]

[a] *Department of Medicine, University of California San Diego, La Jolla, CA, 92093, USA*
[b] *National Center for Microscopy and Imaging Research, Department of Neurosciences, University of California San Diego, La Jolla, CA, 92093, USA*
[c] *Hamilton Glaucoma Center and Shiley Eye Institute, Viterbi Family Department of Ophthalmology, University of California San Diego, La Jolla, CA, 92093, USA*
[d] *Department of Physiology, Biophysics & Ophthalmology, University of California Irvine, Irvine, CA, 92697, USA*

ARTICLE INFO

Keywords:
AIBP
Glaucoma
Neuroinflammation
Müller glia
Retinal ganglion cell
Mitochondria

ABSTRACT

Glaucoma is a leading cause of blindness worldwide in individuals 60 years of age and older. Despite its high prevalence, the factors contributing to glaucoma progression are currently not well characterized. Glia-driven neuroinflammation and mitochondrial dysfunction play critical roles in glaucomatous neurodegeneration. Here, we demonstrated that elevated intraocular pressure (IOP) significantly decreased apolipoprotein A-I binding protein (AIBP; gene name *Apoa1bp*) in retinal ganglion cells (RGCs), but resulted in upregulation of TLR4 and IL-1β expression in Müller glia endfeet. *Apoa1bp*$^{-/-}$ mice had impaired visual function and Müller glia characterized by upregulated TLR4 activity, impaired mitochondrial network and function, increased oxidative stress and induced inflammatory responses. We also found that AIBP deficiency compromised mitochondrial network and function in RGCs and exacerbated RGC vulnerability to elevated IOP. Administration of recombinant AIBP prevented RGC death and inhibited inflammatory responses and cytokine production in Müller glia *in vivo*. These findings indicate that AIBP protects RGCs against glia-driven neuroinflammation and mitochondrial dysfunction in glaucomatous neurodegeneration and suggest that recombinant AIBP may be a potential therapeutic agent for glaucoma.

1. Introduction

Glaucoma is a leading cause of irreversible blindness worldwide in individuals 60 years of age and older. Despite the high prevalence of glaucoma, the factors contributing to its progressive worsening are currently not well characterized. To date, intraocular pressure (IOP) is the only proven treatable risk factor. Eye drops or systemic administration of medications are employed to lower IOP. However, lowering IOP often is insufficient for preventing disease progression. Neuroinflammation is defined as immune responses in the central nervous system, and it is of great interest to better understanding the role of glia-mediated neuroinflammation in glaucoma [1,2]. However, the interplay between glia-mediated neuroinflammation and mitochondrial dysfunction in glaucomatous neurodegeneration is poorly understood.

Apolipoprotein A-I binding protein (AIBP; gene name *APOA1BP*) is a secreted protein that associates with apolipoprotein A-I (APOA-I) [3] and high-density lipoprotein (HDL) [4]. Human *APOA1BP* mRNA is ubiquitously expressed, and the AIBP protein is found in cerebrospinal fluid and urine [3,5,6]. We and others have demonstrated that the binding of AIBP to HDL facilitates cholesterol efflux from endothelial cells and macrophages, resulting in reduction of lipid rafts, inhibition of angiogenesis and atherosclerosis, and regulation of hematopoietic stem

---

* Corresponding author.
** Corresponding author.
E-mail addresses: soc002@health.ucsd.edu (S.-H. Choi), wju@health.ucsd.edu (W.-K. Ju).

[1] Soo-Ho Choi and Keun-Young Kim contributed equally to this work.

[2] Current address of Genea Edwards is Vision Research Center, Department of Ophthalmology, University of Missouri-Kansas City, Kansas City, Missouri 64110, USA.

[3] The Ju and Miller laboratories contributed equally to this work.

https://doi.org/10.1016/j.redox.2020.101703
Received 13 July 2020; Received in revised form 12 August 2020; Accepted 22 August 2020

and progenitor cell fate [4,7–9]. More recently, we have shown that AIBP binds Toll-like receptor-4 (TLR4), thus mediating selective regulation of lipid rafts in activated cells. It also inhibits TLR4 dimerization, neuroinflammation, and glial activation in the mouse models of neuropathic pain states [10,11]. These findings demonstrate a mechanism by which AIBP regulates neuroinflammation and suggest a therapeutic potential of AIBP for treating neuropathic pain [10].

TLR4 is an important innate immune receptor that contributes to the innate and adaptive inflammatory responses. Upon activation, TLR4 is recruited to lipid rafts where it dimerizes and initiates a signaling cascade leading to proinflammatory responses [11–13]. Previous studies have demonstrated that TLR4-dependent signaling induces the IL-1β cascade in elevated IOP-induced acute glaucoma [14,15]. Evidence from our group and others strongly indicates that mitochondrial dysfunction and metabolic stress by glaucomatous insults such as elevated IOP and oxidative stress are critical to loss of RGCs in experimental glaucoma [16–19]. TLR4 is also associated with mitochondrial damage caused by intracellular reactive oxygen species (ROS) and defective mitochondrial dynamics [20,21]. In transfected cells, AIBP is reported to localize to mitochondria [22], but potential mechanisms connecting AIBP, TLR4 signaling, mitochondrial dysfunction, and neuroinflammation in glaucoma remain to be elucidated.

Here, we demonstrate that AIBP plays a critical role in protection against neuroinflammation and mitochondrial dysfunction during glaucomatous neurodegeneration. Using systemic AIBP knockout (*Apoa1bp*$^{-/-}$) mice, we show that AIBP deficiency triggers mitochondrial dysfunction in both RGCs and Müller glia. It also increases TLR4 and IL-1β expression in Müller glia endfeet, leading to oxidative stress, RGC death and visual dysfunction. Moreover, AIBP deficiency exacerbates vulnerability to elevated IOP-induced RGC death. In particular, AIBP treatment inhibits inflammatory responses and protects RGCs against elevated IOP. These results suggest that AIBP has therapeutic potential for restraining excessive mitochondrial dysfunction and neuroinflammation in glaucomatous neurodegeneration.

2. Materials and methods

2.1. Human tissue samples

Human retina tissue sections were obtained from a normal (age 81 years) donor and a patient with glaucoma (age 91 years) (San Diego Eye Bank, CA, USA) with a protocol approved by the University of California, San Diego Human Research Protection Program. The normal patient has no history of eye disease, diabetes, or chronic central nervous system disease.

2.2. Animals

Adult male and female DBA/2J and age-matched DBA/2J-*Gpnmb*$^{+}$ (D2-*Gpnmb*$^{+}$) mice (The Jackson Laboratory, ME, USA), and WT and Apoa1bp$^{-/-}$ mice were housed in covered cages, fed with a standard rodent diet ad libitum, and kept on a12 h light/12 h dark cycle. C57BL/6J mice were initially purchased from the Jackson Laboratory, bred in-house for experiments and used as wild-type (WT) mice. *Apoa1bp*$^{-/-}$ mice on a C57BL/6J background were generated in our group as previously reported [8,23]. Animals were assigned randomly to experimental and control groups. To investigate the effect of IOP elevation and/or AIBP deficiency, 10 month-old DBA/2J and age-matched D2-*Gpnmb*$^{+}$ mice, and 4 month-old WT and age-matched *Apoa1bp*$^{-/-}$ mice were used. Behavioral response and visual function were studied with 3–4 month old male and female mice. All procedures concerning animals were in accordance with the Association for Research in Vision and Ophthalmology Statement for the Use of Animals in Ophthalmic Vision Research and under protocols approved by Institutional Animal Care and Use Committee at the University of California, San Diego (USA).

2.3. Induction of acute IOP elevation

Mice were anesthetized by an intraperitoneal (IP) injection of a cocktail of ketamine (100 mg/kg, Ketaset; Fort Dodge Animal Health, IA, USA) and xylazine (9 mg/kg, TranquiVed; VEDCO Inc., MO, USA). Eyes were also treated with 1% proparacaine drops. Induction of acute IOP elevation was performed as previously described [24]. Briefly, a 30-gauge needle was inserted into the anterior chamber of right eye that was connected by flexible tubing to a saline reservoir. By raising the reservoir, IOP was elevated to 70–80 mmHg for 50 min. Sham treatment was performed in the contralateral eyes by the insertion of a needle in the anterior chamber without saline injection. Recirculation started immediately after removal of the cannula and the IOP decreased to normal values within 5 min. Mice were anesthetized by an IP injection of a cocktail of ketamine/xylazine as described above prior cervical dislocation at different time points for tissue preparation after reperfusion: 1 day and 4 weeks. Retinal ischemia was confirmed by observing whitening of the iris and loss of the retina red reflex. IOP was measured with a tonometer (icare TONOVET, Vantaa, Finland) during IOP elevation. Non-IOP elevation contralateral control retinas were used as sham control.

2.4. IOP measurement

IOP elevation onset typically occurs between 5 and 7 months of age, and by 9–10 months of age, IOP-linked optic nerve axon loss is well advanced [16,25]. IOP measurement was performed as previously described [16,25]. The glaucomatous DBA/2J mice that have confirmed IOP elevation were obtained in 65.3% (64/98) at 10 months of age [25]. Our previous study showed that mean IOP was 15 ± 1.8 mmHg in 3 month-old DBA/2J mice and that spontaneous IOP elevation typically began by 6–8 months. The peak of IOP elevation was 21.5 ± 4.5 mmHg in the right eyes and 19.9 ± 3.7 mmHg in the left eyes within 10 month-old DBA/2J mice [25]. As has been reported previously [26,27], substantial ON damage, including axon loss, was observed in 10 month-old glaucomatous DBA/2J mice, confirming the presence of acquired optic neuropathy. Each of the 10 month-old DBA/2J mice used in this study had a single IOP measurement (to confirm development of spontaneous IOP elevation exceeding 20 mmHg) (n = 5 for selected DBA/2J mice). Also, each of the non-glaucomatous control C57BL/6 or D2-*Gpnmb*$^{+}$ mice (n = 5) used in this study had a single IOP measurement. For WT and *Apoa1bp*$^{-/-}$ mice, IOP was measured with a tonometer (icare TONOVET) as described above.

2.5. Cell culture and hydrostatic pressure (HP) system in vitro

RGCs from postnatal 5 days of Sprague-Dawley rat were purified by immunopanning and were cultured in serum-free defined growth medium as previously described [16]. Approximately 2 × 10^5 purified cells were seeded on 60 mm dishes coated first with poly-D-lysine (70 kDa, 10 μg/ml; Sigma, MO, USA) and then with laminin (10 μg/ml; Sigma) in neurobasal medium. RGCs were cultured in serum-free defined growth medium containing BDNF (50 μg/ml; Sigma), CNTF (10 μg/ml; Sigma), insulin (5 μg/ml; Sigma), and forskolin (10 μg/ml; Sigma). A pressurized incubator was used to expose the cells to elevated HP as previously described [16]. The plexiglass pressure chamber was connected via a low-pressure two-stage regulator (Gilmont Instruments, Barnant Company, IL, USA) to a certified source of 5% CO_2/95% air (Airgas Inc., CA, USA).

2.6. Recombinant AIBP

N-terminal His-tagged AIBP was produced in a baculovirus/insect cell expression system to allow for post-translational modification and to ensure endotoxin-free preparation as previously described [9,11]. AIBP protein was purified using a Ni-NTA agarose column (Qiagen, CA, USA) eluted with imidazole. Purified AIBP was dialyzed against PBS, and concentration was measured. Aliquots were stored at −80 °C.

2.7. Tissue preparation

Mice were anesthetized by an IP injection of a cocktail of ketamine/xylazine as described above prior cervical dislocation. For immunohistochemistry, the retinas and superior colliculus (SC) tissues were dissected from the choroids and fixed with 4% paraformaldehyde (Sigma) in phosphate buffered saline (PBS, pH 7.4, Sigma) for 2 h at 4 °C. Retinas and SCs were washed several times with PBS then dehydrated through graded levels of ethanol and embedded in polyester wax. For EM, the eyes were fixed via cardiac perfusion with 2% paraformaldehyde, 2.5% glutaraldehyde (Ted Pella, CA, USA) in 0.15 M sodium cacodylate (pH 7.4, Sigma) solution at 37 °C and placed in precooled fixative of the same composition on ice for 1 h. As described below, the procedure was used to optimize mitochondria structural preservation and membrane contrast. For Western blot and PCR analyses, extracted retinas were immediately used.

2.8. Western blot analyses

Harvested retinas were homogenized for 1 min on ice with a modified RIPA lysis buffer (#9806, Cell Signaling Technology, MA, USA), containing complete protease inhibitor cocktail (#HY-K0010, MedChemExpress, NJ, USA). The lysates were then centrifuged at 15,000 g for 15 min and protein amounts in the supernatants were measured by Bradford assay. Proteins (10–20 μg) were run on a NuPAGE Bis-Tris gel (Invitrogen, CA, USA) and transferred to polyvinylidene difluoride membranes (GE Healthcare Bio-Science, NJ, USA). The membranes were blocked with 5% non-fat dry milk and PBS/0.1% Tween-20 (PBS-T) for 1 h at room temperature and incubated with primary antibodies (sTable 1) for overnight at 4 °C. Membrane were washed three times with PBS-T then incubated with horseradish peroxidase-conjugated secondary antibodies (Bio-Rad, CA, USA) for 1 h at room temperature. Membranes were developed using enhanced chemiluminescence substrate system. The images were captured using a UVP imaging system (UVP LLC, CA, USA).

2.9. Immunohistochemistry

Immunohistochemical staining of 7 μm wax sections of full thickness retina were performed. Sections from wax blocks from each group ($n = 4$ retinas/group) were used for immunohistochemical analysis. To prevent non-specific background, tissues were incubated in 1% bovine serum albumin (BSA, Sigma)/PBS for 1 h at room temperature before incubation with the primary antibodies for 16 h at 4 °C. After several wash steps, the tissues were incubated with the secondary antibodies (sTable 1) for 4 h at 4 °C and subsequently washed with PBS. The sections were counterstained with the nucleic acid stain Hoechst 33342 (1 μg/ml; Invitrogen) in PBS. Images were acquired with Olympus FluoView1000 confocal microscopy (Olympus, Tokyo, Japan) or Leica SPE-II confocal microscope (Leica, Wetzlar, Germany). Each target protein fluorescent integrated intensity in pixel per area was measured using the ImageJ software. All imaging parameters remained the same and were corrected with the background subtraction.

2.10. Terminal deoxynucleotidyl transferase dUTP nick end labeling (TUNEL) staining

TUNEL staining was performed using *In Situ* Cell Detection Kit (TMR red, Roche Biochemicals, IN, USA) as previously described [28,29]. After rinsing in PBS, the sections were incubated with TUNEL mixture in reaction buffer for 60 min at 37 °C. To count TUNEL-positive cells, the areas were divided into three layers by ganglion cell layer (GCL), inner nuclear layer (INL) and outer nuclear layer (ONL). To determine whether TUNEL-positive cells are RGCs, we performed immunohistochemistry before TUNEL staining using RNA-binding protein with multiple splicing (RBPMS) antibody as described above. The sections were counterstained with the Hoechst 33342 (1 μg/ml; Invitrogen) in PBS as described above. TUNEL-positive cells were counted in 5 microscopic fields (20x) per condition ($n = 5$ retinas) by two investigators in a masked fashion, and the scores were averaged. Images were acquired with Olympus FluoView1000 confocal microscopy (Olympus).

2.11. Whole-mount immunohistochemistry and RGC counting

Retinas from enucleated eyes were dissected as flattened whole-mounts from WT and *Apoa1bp*$^{-/-}$ mice. Retinas were immersed in PBS containing 30% sucrose for 24 h at 4 °C. The retinas were blocked in PBS containing 3% donkey serum, 1% bovine serum albumin, 1% fish gelatin and 0.1% Triton X-100, and incubated with primary antibodies (sTable 1) for 3 days at 4 °C. After several wash steps, the tissues were incubated with the secondary antibodies (sTable 1) for 24 h, and subsequently washed with PBS. Images were captured under fluorescence microscopy using a Nikon ECLIPSE microscope (E800; Nikon Instruments Inc., NY, USA) equipped with digital camera (SPOT Imaging, MI, USA) or Olympus FluoView1000 confocal microscopy (Olympus). Image exposures were the same for all tissue sections and were acquired using Simple PCI version 6.0 software (Compix Inc.). To count RGCs labeled with Brn3a, each retinal quadrant was divided into three zones by central, middle, and peripheral retina (one sixth, three sixths, and five sixths of the retinal radius). RGC densities were measured in 12 distinct areas (one area at central, middle, and peripheral per retinal quadrant) per condition by two investigators in a masked fashion, and the scores were averaged.

2.12. Serial block-face scanning electron microscopy (SBEM)

Retina tissues were washed with cacodylate buffer for 2 h at 4 °C and then placed into cacodylate buffer containing 2 mM $CaCl_2$ and 2% OsO_4/1.5% potassium ferrocyanide as previously described [16]. The tissues were left for 2 h at room temperature. After thorough washing in double distilled water, the tissues were placed into 0.05% thiocarbohydrazide for 30 min. The tissues were again washed and then stained with 2% aqueous OsO_4 for 1 h. The tissues were washed and then placed into 2% aqueous uranyl acetate overnight at 4 °C. The tissues were washed with water at room temp and then stained with en bloc lead aspartate for 30 min at 60 °C. The tissues were washed with water and then dehydrated on ice in 50%, 70%, 90%, 100%, 100% ethanol solutions for 10 min at each step. The tissues were then washed twice in dry acetone and then placed into 50:50 Durcupan ACM:acetone overnight. The tissues were transferred to 100% Durcupan resin overnight. The tissues were then embedded and left in an oven at 60 °C for 72 h. BEM was performed on Merlin scanning electron microscopy (Zeiss, Oberkochen, Germany) equipped with a 3view2XP and OnPoint backscatter detector (Gatan, CA, USA). The retina volumes were collected at 2.5 kV accelerating voltages, with pixel dwell time of 0.5 μs The raster size was 20k x 5k, with 3.5 nm pixels and 50 nm z step size. Once a volume was collected, the histograms for the tissues throughout the volume stack were normalized to correct for drift in image intensity during acquisition. Digital micrograph files (.dm4) were normalized using Digital Micrograph and then converted to MRC format. The stacks were converted to eight bit and volumes were manually traced for reconstruction and analysis using IMOD software (http://bio3d.colorado.edu/imod/).

2.13. 3DEM tomography

EM tomography experiments were conducted on a FEI Titan Halo operating in the Scanning Transmission Electron Microscope mode at 300 kV, with the possibility to resolve micrometer thick plastic embedded specimen down to nanoscale spatial resolution as described previously. Vertical sections of retina tissues from each group were cut at a thickness of 750 nm and electron tomography was performed following a 4-tilt series scheme described in, with the specimen tilted from −60° to +60° every 0.5° at four evenly distributed azimuthal angle positions. The magnification was 28,500 × and the pixel resolution was 4.2 nm. The IMOD package was used for alignment, reconstruction and volume segmentation. Volume segmentation was performed by manual tracing of membranes in the planes of highest resolution with the Drawing Tools and Interpolator plug-ins [16,25,30]. The reconstructions and surface-rendered volumes were visualized using 3DMOD. Measurements of mitochondrial outer, inner boundary (IBM), and cristae membrane surface areas and volumes were made within segmented volumes using IMODinfo. These were used to determine the cristae density, defined as the ratio: sum of the cristae membrane surface areas divided by the mitochondrial outer membrane surface area.

2.14. *Energy calculations*

We used the biophysical modeling of Song et al. [31], which takes into account spatially accurate geometric representations of a crista, inner boundary membrane and crista junction to estimate the rate of mitochondrial ATP generation. The validity of this modeling was supported by predicting the higher proton motive force on cristae membranes, the effect of crista surface-to-volume ratio on this force, and the effect of crista membrane surface area on the rate of ATP synthesis—all integral to the current paradigm of mitochondrial structure/function ATP mechanics. The first variable needed in the model is the crista shape factor, defined as the crista membrane surface area divided by the crista volume. Measurements of crista surface area and volume were made from 3DEM mitochondrial volumes using ImageJ measurement tools. The rate of ATP production per crista was derived from Song et al. [31] Fig. 5b, which plots the rate of ATP production as a function of crista surface area for differing values of the crista shape factor. This rate was then summed for all the cristae in a given mitochondrion to produce the ATP rate of production per mitochondrion. Because mitochondria differ in size, the rate of ATP production was also calculated per unit mitochondrial volume (micron^3) after measuring each mitochondrion's volume using ImageJ tools. Also, because mitochondria produce most of their ATP for the cell's use, we calculated the amount of ATP available per second per unit cytoplasmic volume (micron^3) by multiplying the mean value of ATP rate per mitochondrion by the number of mitochondria in the cytoplasmic volume (nucleus excluded) and dividing by the cytoplasmic volume after measuring each cell's volume using ImageJ tools.

There are two caveats with the energy calculations. First, this analysis does not take into account the ATP produced by glycolysis. RGCs appear to favor oxidative phosphorylation [32]. In vitro studies indicate that Müller glia may be predominantly glycolytic. However, Müller glia metabolism may shift from glycolysis to oxidative phosphorylation during stress, such as when energy demand exceeds supply or oxidative stress. Thus, a switch in Müller glia metabolism may be a biomarker for pathophysiology, at least in vitro. Second, mitochondrial respiration can be governed by various states, the most common in vitro being state 3 (active) and state 4 (resting). State 3 respiration can have an ATP production rate up to four times that of state 4. If the *in vivo*, or in our case, *ex vivo* (in silico) energy state follows the in vitro findings, both RGCs and Müller glia mitochondria exhibit state 4 respiration. Taking into consideration the estimates and uncertainties, it is important to understand that the calculations of ATP production rate may have "first-order" accuracy. The ATP production rates of Müller glia endfeet and RGC mitochondria are in agreement with estimations for other cell types [33,34]. Note that the rate of ATP production is higher per mitochondrion for Müller glia endfeet and RGC because their mitochondria are larger, especially compared with the small synaptic mitochondria examined by Garcia and coworkers.

2.15. *Quantitative PCR analyses*

Total RNA from the retina was isolated using Nucleospin RNA columns (Clontech, CA, USA). Isolated RNA was reverse transcribed using RNA to cDNA EcoDry (Clontech) following the manufacturer's instructions. Quantitative PCR (qPCR) was performed using KAPA SYBR FAST Universal qPCR kit (KAPA Biosystems, KK4602, Roche Diagnostics, IN, USA), with primers ordered from Integrated DNA Technologies (IDT, CA, USA), and a Rotor Gene Q thermocycler (Qiagen). The qPCR was performed with cDNAs synthesized from 1 μg of the total RNA of each group as a template and specific primers (sTable 2).

2.16. *Virtual optomotor response analysis*

Spatial visual function was performed on a virtual optomotor system (OptoMotry; CerebralMechanics Inc., AB, Canada) [35]. Unanesthetized mice were placed on an unrestricted platform in the center of a virtual cylinder comprised of four monitors arranged in a square (arena) that project a sinusoidal grating (i.e., white versus black vertical bars) rotating at 12 deg/sec. Mice were monitored by a camera mounted at the top of the arena while a cursor placed on the forehead centers the rotation of the cylinder at the animal's viewing position. To assess visual acuity, tracking was determined when the mouse stops moving its body and only head-tracking movement is observed. Spatial frequency threshold, a measure of visual acuity, was determined automatically with accompanying OptoMotry software, which uses a step-wise paradigm based upon head-tracking movements at 100% contrast. Spatial frequency began at 0.042 cyc/deg, which gradually increased until head movement was no longer observed.

2.17. *Visual evoked potential (VEP) analysis*

VEP was measured as previously described [36,37]. Mice were dark adapted in the procedure room at vivarium for less than 12 h in a dark room. Mice were prepared for recording under dim red light and anesthetized with IP injection of a mixture of ketamine/xylazine as described above. Pupils were dilated using equal parts of topical phenylephrine (2.5%) and tropicamide (1%). Proparacaine (0.5%) was used as a topical anesthetic to avoid blinking and a drop of lubricant is frequently applied on the cornea to prevent dehydration and allow electrical contact with the recording electrode (a gold wire loop, disposable). The top of the mouse's head was cleaned with an antiseptic solution. A scalpel was used to incise the scalp skin, and a metal electrode was inserted into the primary visual cortex through the skull, 0.8 mm deep from the cranial surface, 2.3 mm lateral to the lambda. A platinum subdermal needle (Grass Telefactor) was inserted through the animal's mouth as a reference and through the tail as ground. The measurements commenced when the baseline waveform became stable, 10–15 s after attaching the electrodes. Flashes of light at 2 log cd.s/m2 were delivered through a full-field Ganzfeld bowl at 2 Hz. Signal was amplified, digitally processed by the software (Veris Instruments, OR, USA), then exported, and peak-to-peak responses were analyzed in Excel (Microsoft). To isolate VEP of the measured eye from the crossed signal originating in the contralateral eye, a black aluminum foil eyepatch was placed over the eye not undergoing measurement. For each eye, peak-to-peak response amplitude of the major component P1–N1 in IOP eyes was compared to that of their contralateral non-IOP controls. The All the recordings are carried out with the same stimulus intensity. The average signals for each group were compared with respect to both amplitude and latency.

2.18. *Cholera toxin-B (CTB) labeling*

Mice were anesthetized with IP injection of a mixture of ketamine/xylazine as described above and topical 1% proparacaine eye drops. A Hamilton syringe was used to inject a 1 μL of Alexa Fluor 594-conjugated CTB (Invitrogen), into the vitreous humor. Injections were given slowly over 1 min and the needle was maintained in position for an additional 5 min to minimize CTB loss through the injection tract. At 3 days after injection, the mice were fixed via cardiac perfusion with 4% paraformaldehyde (Ted Pella) following an IP injection of a mixture of ketamine/xylazine. After perfusion, the SC tissues were dissected and immersed in PBS containing 30% sucrose for 24 h at 4 °C. The SC tissues were coronally sectioned at 50 μm using a Leica Cryostat (Wetzlar, Germany). The 30 representative sections were mounted on slides and images were acquired with Olympus FluoView1000 (Olympus). The area densities from the images were analyzed using ImageJ (http://rsb.info.nih.gov/ij/; provided in the public domain by the National Institutes of Health, MD, USA) and Imaris software (Bitplane Inc., MA, USA).

2.19. Statistical analysis

For comparison between two groups that have small number of samples related to a fixed control, statistical analysis was performed using the nonparametrical analysis to one-sample *t*-test. For comparison between independent two groups, a two-tailed Student's *t*-test was performed. For multiple group comparisons, we used either one-way ANOVA or two-way ANOVA, using GraphPad Prism (GraphPad, CA, USA). A *P* value less than 0.05 was considered statistically significant.

3. Results

3.1. Reduced AIBP expression in RGCs in glaucomatous retinas

In neonatal mice, *Apoa1bp* mRNA is expressed in RGCs [8]. To determine whether elevated pressure alters expression level of AIBP in murine RGCs, we first transiently induced acute IOP elevation in the eye of normal C57BL/6J mice by the cannulation of the anterior chamber of the eye, which was elevated to maintain an IOP of 70–80 mmHg for 50 min [24]. This model is also widely used by others to determine RGC death and survival in degenerative retinal diseases including acute glaucoma [14,38]. We found that elevated IOP significantly reduced *Apoa1bp* gene and AIBP protein expression in the retina at 24 h compared with sham control retina (Fig. 1A and B). Immunohistochemical analysis showed that AIBP immunoreactivity was localized in the outer plexiform layer (OPL), INL, inner plexiform layer (IPL), and GCL of control mice. In the GCL, AIBP immunoreactivity was present in RGC somas and axons, which were labeled with neuron-specific β-III tubulin (TUJ1), a marker for RGCs. Consistently, elevated IOP decreased AIBP immunoreactivity in the OPL and inner retinal layer (Fig. 1C). We further cultured primary RGCs and exposed cells to elevated HP (30 mmHg) for 3 days [16]. Notably, elevated HP exposure significantly reduced AIBP protein expression in RGCs (Fig. 1D).

We next examined whether a chronic IOP elevation alters AIBP protein expression in the retina using glaucomatous DBA/2J mice, which spontaneously develop elevated IOP and glaucomatous damage with age, and age-matched control D2-*Gpnmb*$^+$ mice [39,40]. Interestingly, we found that glaucomatous DBA/2J retina showed a similar pattern of reduced AIBP immunoreactivity as in our acute model of IOP elevation (Fig. 1E). In D2-*Gpnmb*$^+$ mice, AIBP immunoreactivity was present not only in RGC soma in the GCL but also in the IPL (Fig. 1F). In contrast, AIBP immunoreactivity was significantly decreased in the inner retina of glaucomatous DBA/2J mice (Fig. 1F and G). Since AIBP mediates the stabilization of ATP-binding cassette transporter A1 (ABCA1) by facilitating apoA-1 binding to ABCA1 and prevents ABCA1 degradation via the ubiquitination pathway [41], we further tested whether a chronic IOP elevation also alters expression level of ABCA1 protein. In D2-*Gpnmb*$^+$ mice, ABCA1 immunoreactivity was present in Brn3a-positive RGCs in the GCL and OPL (Fig. 1H). In contrast, ABCA1 immunoreactivity was highly diminished in the neurons of the GCL, including Brn3a-positive RGCs, of glaucomatous DBA/2J retina (Fig. 1H and I).

3.2. AIBP deficiency exacerbates RGC vulnerability to elevated IOP and triggers visual dysfunction

To test the hypothesis that AIBP deficiency plays an important role in glaucomatous RGCs, we used *Apoa1bp*$^{-/-}$ mice that are viable and fertile, and have no apparent morphological defects compared with control mice under naïve conditions [8]. As shown in Fig. 2, we induced IOP elevation in WT and *Apoa1bp*$^{-/-}$ mice and assessed RGC loss at 4 weeks after IOP elevation. There was no statistically significant difference in IOPs between WT and naïve *Apoa1bp*$^{-/-}$ mice. The mean IOP of contralateral control eyes was 9–10 mmHg and IOP was elevated in ipsilateral eyes to 70–75 mmHg in WT and *Apoa1bp*$^{-/-}$ mice ($n = 15$ mice; Fig. 2A). Remarkably, we found that elevated IOP significantly enhanced RGC loss in all retinal areas of *Apoa1bp*$^{-/-}$ mice compared with sham control WT or naïve *Apoa1bp*$^{-/-}$ retinas (Fig. 2B and C). In addition, we observed that no statistically significant differences in RGC number were detected in the retinas between sham control WT and naïve *Apoa1bp*$^{-/-}$ mice (Fig. 2B and C).

To test the effect of AIBP deficiency on visual function, we next measured 1) the maximum spatial frequency that could elicit head tracking ("acuity") in a virtual-reality optomotor system and 2) central visual function using VEP, a measurement of the electrical signal recorded at the scalp over the occipital cortex in response to light stimulus. In the absence of AIBP, we found a significant reduction of visual acuity by decreasing spatial frequency in both male and female naïve *Apoa1bp*$^{-/-}$ mice (Fig. 2D). However, there were no statistically significant differences in VEP P1–N1 potentials and latency in naïve *Apoa1bp*$^{-/-}$ mice compared with WT mice (Fig. 2E and F). Because VEP is considered to be valid in analyzing and predicting visual properties in glaucoma patients with severe visual impairments [42], our results suggest the possibility that while AIBP deficiency triggers spatial vision dysfunction in the eye, it may not be sufficient to induce severe progression of optic nerve damage. Additionally, we further determined whether AIBP deficiency alters axon transport from retina to SC by intravitreal injection of an anterograde tracer, CTB, into the eyes of WT and naïve *Apoa1bp*$^{-/-}$ mice. At 3 days after injection, we measured anterograde tracing of CTB to SC. We found that there was no statistically significant difference in the density of CTB labeling in the SC between WT and naïve *Apoa1bp*$^{-/-}$ mice (Fig. 2G and H).

3.3. Increased TLR4 and IL-1β expression in glaucomatous and Apoa1bp$^{-/-}$ müller glia endfeet

AIBP plays a unique role of targeting cholesterol efflux machinery to TLR4-occupied inflammarafts [10,11]. Evidence from clinical and animal studies indicates that TLR4-dependent signaling is an important factor in the pathogenesis of POAG and that this signaling is associated with activated glial cells and contributes to inflammatory responses in experimental glaucoma [43–45]. First, we determined the expression level and distribution of TLR4 and IL-1β proteins in glaucomatous retinas from human patients with POAG and DBA/2J mice. Remarkably, we observed significantly increased patterns of TLR4 and IL-1β immunoreactivity in glutamine synthase (GS)-positive Müller glia in both glaucomatous human and DBA/2J mouse retinas compared with control retinas (Fig. 3A and B). In glaucomatous human retina, we found that TLR4 immunoreactivity was increased in the endfeet of Müller glia of the GCL and nerve fiber layer (NFL) compared with normal retina, while IL-1β immunoreactivity was increased in both processes and endfeet of Müller glia of the IPL, GCL and NFL (Fig. 3A and B). In glaucomatous DBA/2J mouse retina, both TLR4 and IL-1β immunoreactivities were significantly increased in the endfeet of Müller glia of the GCL but depleted in the processes of Müller glia compared with age-matched control D2-*Gpnmb*$^+$ mouse retina (Fig. 3A and B). Consistent with these results, glaucomatous retinas displayed significantly increased relative fluorescence intensity of both TLR4 and IL-1β proteins in the endfeet of Müller glia in the GCL compared with control Müller glia

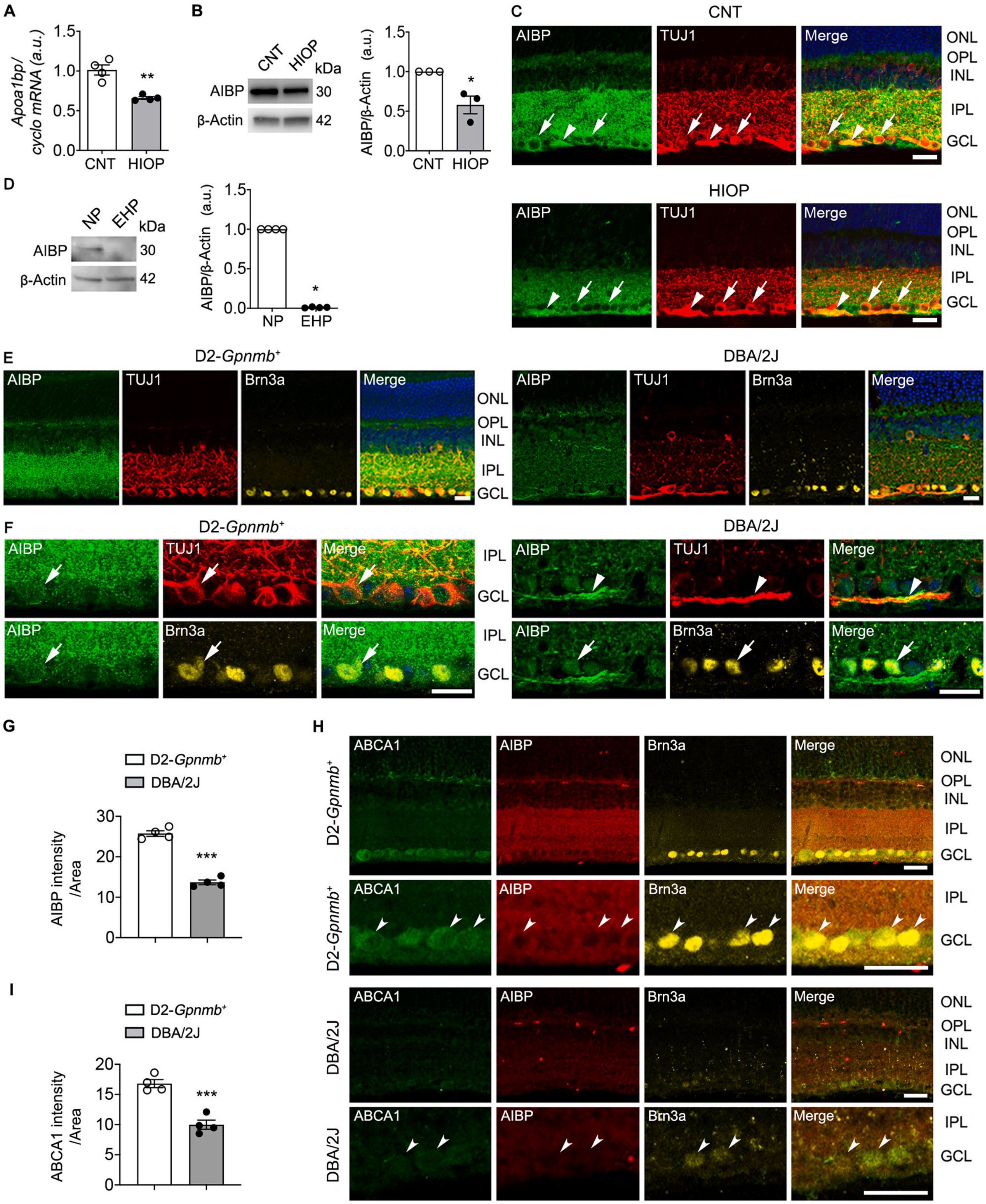

(caption on next page)

Fig. 1. AIBP expression is decreased in glaucomatous retinas and pressure-induced RGCs. (*A*) *Apoa1bp* gene expression in control and injured retina at 1 day after acute IOP elevation. $N = 4$ mice. (*B*) AIBP protein expression in control and injured retina at 1 day after acute IOP elevation. $N = 3$ mice. (*C*) Representative images showed AIBP (green) and TUJ1 (red) immunoreactivities at 1 day after acute IOP elevation. Arrows indicate AIBP immunoreactivity co-labeled with TUJ1 in RGC somas and arrowhead indicates AIBP co-labeled with TUJ1 in RGC axon bundle. (*D*) AIBP protein expression in control and injured RGCs at 3 day after elevated HP. $n = 3$ independent experiments with cultures. (*E*) Representative images showed AIBP (green), TUJ1 (red) and Brn3a (yellow) immunoreactivities. (*F*) In higher magnification images, arrows indicate AIBP immunoreactivity co-labeled with TUJ1 in RGC somas and arrowhead indicates AIBP co-labeled with TUJ1 in RGC axon bundle. (*G*) Quantitative fluorescent intensity showed a significant decrease in AIBP immunoreactivity in the inner retina of glaucomatous DBA/2J mice. $N = 4$ mice. (*H*) Representative images showed ABCA1 (green), AIBP (red) and Brn3a (yellow) immunoreactivities. Concave arrowheads indicate ABCA1-positive RGCs co-labeled with AIBP and Brn3a. (*I*) Quantitative fluorescent intensity showed a significant decrease in ABCA1 immunoreactivity in the GCL of glaucomatous DBA/2J mice. $N = 4$ mice. Error bars represent SEM. Statistical significance determined using Student's *t*-test. $^{*}P < 0.05$; $^{**}P < 0.01$; $^{***}P < 0.001$. Blue is Hoechst 33342 staining. Scale bar: 20 μm. CNT, control; GCL, ganglion cell layer; HIOP, high intraocular pressure; EHP, elevated hydrostatic pressure; INL, inner nuclear layer; IPL, inner plexiform layer; N'P, no pressure; ONL, outer nuclear layer; OPL, outer plexiform layer. (For interpretation of the references to colour in this figure legend, the reader is referred to the Web version of this article.)

(Fig. 3C and D). Second, we further determined whether AIBP deficiency alters TLR4 and IL-1β protein expression in Müller glia using *Apoa1bp*$^{-/-}$ mice. We found that AIBP deficiency not only significantly increased TLR4 and IL-1β immunoreactivities in the endfeet of Müller glia in the GCL but also showed a characteristic pattern of increased TLR4 and IL-1β expression in the processes of Müller glia in the IPL observed in DBA/2J mouse and human glaucomatous retina (Fig. 3A–D).

3.4. AIBP deficiency induces mitochondrial fragmentation and reduces ATP production in müller glia

TLR4 is associated with mitochondrial damage caused by intracellular ROS and defective mitochondrial dynamics [20,21]. Using naïve *Apoa1bp*$^{-/-}$ mice, we further investigated whether AIBP contributes to the regulation of mitochondrial structure and function in the endfeet of Müller glia. 3D EM (Fig. 4A and B, and sFig. 1) demonstrated lower crista density and dark outer membrane onion-like swirls in *Apoa1bp*$^{-/-}$ mitochondria (Fig. 4B and sFig. 1D), although fewer in number than found in the RGC. Interestingly, we also found ring-shaped mitochondria, a hallmark of mitochondrial stress (sFig. 1E) [46], as well as lower rough endoplasmic reticulum (ER) density and dilated ER strands (sFig. 1D and E). The mitochondria were traced in yellow to make it easier to identify them and those with lower crista density pointed to in *Apoa1bp*$^{-/-}$ (Fig. 4B and sFig. 1). Mitochondria in the Müller glia have rarely been studied via EM at high resolution or in 3D in a quantitative manner [47]. Reconstructions showed examples of long tubular mitochondria in WT but small rounded mitochondria in *Apoa1bp*$^{-/-}$ (Fig. 4C and D, and sMovies 1 and 2). Because each mitochondrion covered multiple image planes at variable cutting angles (Fig. 4E and F), to perform more accurate length measurement, mitochondria were segmented by drawing a series of connected spheres centered along the length of each mitochondrion using IMOD open contour (Fig. 4G–I). Measurements of mitochondria showed that there were no significant changes in mitochondrial volume (Fig. 4J, $n = 50$ mitochondria in 5 Müller glia endfeet), volume density (Fig. 4K, $n = 10$ Müller glia endfeet), or mitochondrial number (Fig. 4L and 10 Müller glia endfeet) in the *Apoa1bp*$^{-/-}$. The form factor for the *Apoa1bp*$^{-/-}$ mitochondria was significantly lower than for the WT (Fig. 4M, $n = 50$ mitochondria in 5 Müller glia endfeet), meaning more mitochondrial rounding in the *Apoa1bp*$^{-/-}$. Interestingly, mitochondrial length was significantly decreased in *Apoa1bp*$^{-/-}$ (Fig. 4N, $n = 50$ mitochondria in 5 Müller glia endfeet). Similarly, the crista density (Fig. 4O, $n = 50$ mitochondria in 5 Müller glia endfeet) and the modeled rate of ATP production per mitochondrial volume (Fig. 4P, $n = 50$ mitochondria in 5 Müller glia endfeet) were lower in the *Apoa1bp*$^{-/-}$. In contrast, the modeled rate of ATP production per mitochondrion was not lower in the *Apoa1bp*$^{-/-}$ (Fig. 4Q, $n = 50$ mitochondria in 5 Müller glia endfeet), yet there was a significant decrease in cellular ATP production via mitochondria in the *Apoa1bp*$^{-/-}$ Müller glia endfeet (Fig. 4R and 10 Müller glia endfeet). Together, these results suggest that AIBP deficiency triggers mitochondrial fragmentation, depletes mitochondrial cristae, and compromises energy production that may lead to dysfunction of Müller glia and activation of inflammatory responses.

Supplementary video related to this article can be found at https://doi.org/10.1016/j.redox.2020.101703

3.5. AIBP deficiency impairs mitochondrial dynamics and OXPHOS activity in the retina

AIBP in transfected cells was shown to localize to mitochondria [22]. At 24 h after acute IOP elevation, we found AIBP protein expression was significantly decreased in the mitochondrial fraction (Fig. 5A), indicating that elevated IOP alters mitochondrial AIBP expression. Thus, we further determined the effect of AIBP deficiency on mitochondrial dynamics and function in the retina. We first found significant decreases of the mitochondrial fusion proteins optic atrophy type 1 (OPA1) and mitofusin 2 (MFN2) in naïve *Apoa1bp*$^{-/-}$ retina compared with WT retina (Fig. 5B). In WT retina, we observed that OPA1 immunoreactivity was highly present in Brn3a-positive RGCs, colocalizing with cytochrome *c* immunoreactivity (Fig. 5C). In contrast, AIBP deficiency diminished OPA1 immunoreactivity in the OPL and INL, as well as RGCs of the GCL (Fig. 5C). Interestingly, we also observed that AIBP deficiency induced an increase of OPA1 immunoreactivity in GS-positive Müller glia (sFig. 2A). In the absence of AIBP, we next found significant decreases of the levels of total mitochondrial fission protein, dynamin-related protein 1 (DRP1), and phosphorylated DRP1 at serine 637 in the retina (Fig. 5D). Immunohistochemical analysis showed that DRP1 immunoreactivity was highly present in the IPL and Brn3a-positive RGCs of the GCL in WT retina (Fig. 5E). In the absence of AIBP, we consistently observed that total DRP1 immunoreactivity was diminished in the OPL and inner retinal layer, especially in RGC somas and the IPL (Fig. 5E). In contrast to Fig. S2A, DRP1 immunoreactivity was not detectable in *Apoa1bp*$^{-/-}$ Müller glia (sFig. 2B). Additionally, there were no statistically significant differences in mitochondrial dynamics-related gene expression (*Opa1, Mfn2* and *Drp1*) between WT and naïve *Apoa1bp*$^{-/-}$ retinas (sFig. 3A). We further determined whether AIBP is involved in mitochondrial OXPHOS in the retina and found that OXPHOS complexes (Cxs) protein expression were significantly decreased in *Apoa1bp*$^{-/-}$ retina (Fig. 5F).

3.6. AIBP deficiency triggers mitochondrial fragmentation and reduces ATP production in RGCs

To determine whether AIBP deficiency directly affects mitochondrial structure and function in RGCs, we assessed the structural and functional changes of mitochondria in *Apoa1bp*$^{-/-}$ RGC somas. Applying 3DEM, we found that AIBP deficiency principally caused swelling and rounding of mitochondria and altered ER structure in RGC somas (Fig. 6A and B and sFig. 4A and B). Even though many of the ER strands were dilated, a hallmark of ER stress, ER-facilitated mitochondrial fission did not appear to be impaired (Fig. 6C–F and sFig. 4B). As with the Müller glia endfeet, abnormal mitochondria with localized structural perturbation of the outer membrane, usually manifest as onion-like

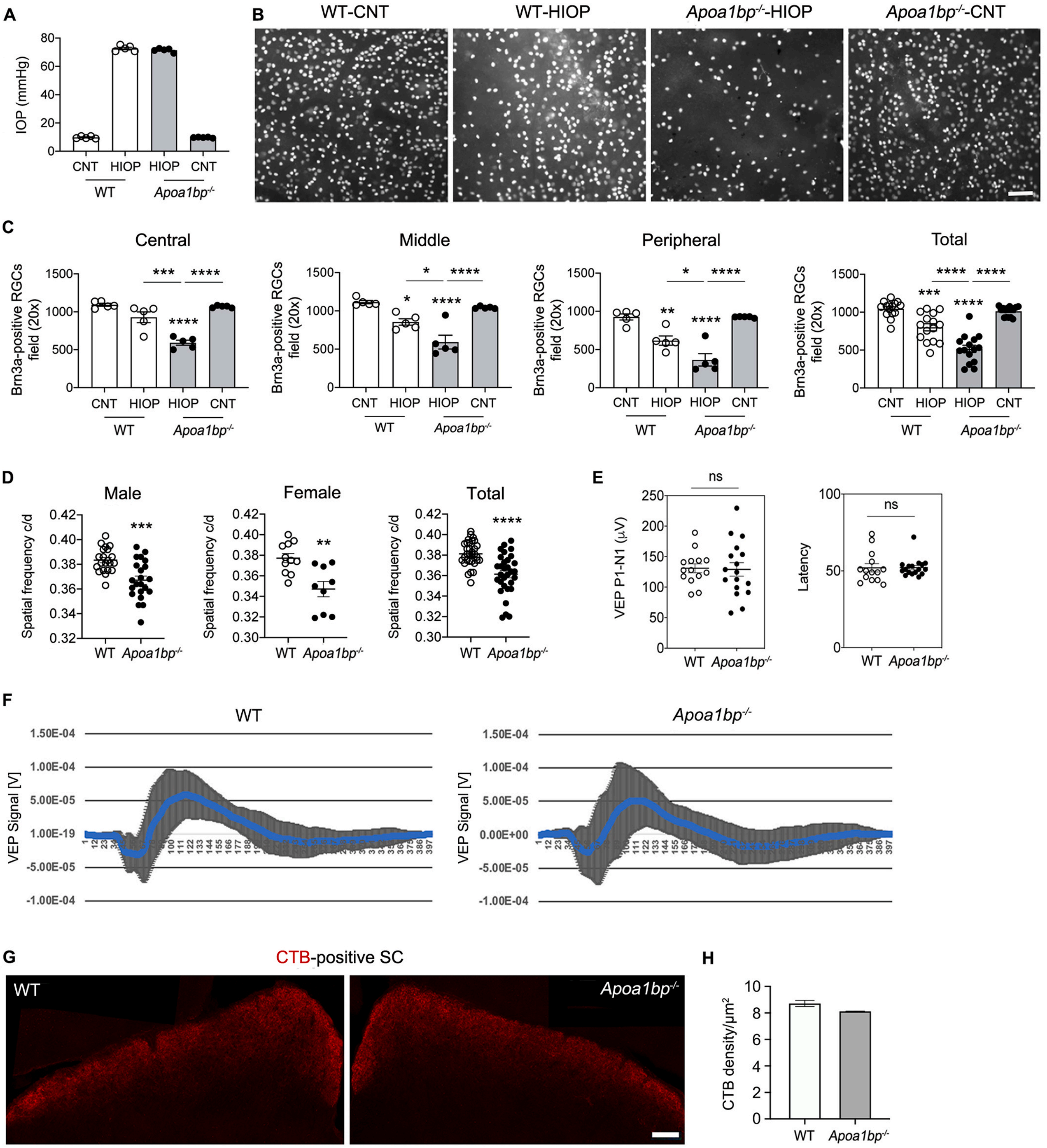

Fig. 2. AIBP deficiency exacerbates vulnerability to elevated IOP in RGCs and triggers visual dysfunction. RGC loss was measured in the retina of 4 month-old WT and age-matched *Apoa1bp*$^{-/-}$ mice at 4 weeks after acute IOP elevation, and visual function were measured in 4-month-old *Apoa1bp*$^{-/-}$ mice. (*A*) The average of IOP elevation in WT mice. $N = 5$–7 mice. (*B*) Representative images from whole-mount immunohistochemistry showed Brn3a-positive RGCs in WT and *Apoa1bp*$^{-/-}$ following acute IOP elevation. (*C*) Quantitative analysis by RGC counting using whole-mount immunohistochemistry for Brn3a in WT and *Apoa1bp*$^{-/-}$ following acute IOP elevation. $N = 5$–7 mice. (*D*) Visual function test in WT and naïve *Apoa1bp*$^{-/-}$ mice by optomotor response analyses. $N = 10$–15 mice. (*E*) Visual function test in WT and naïve *Apoa1bp*$^{-/-}$ mice by VEP analyses. Note that there were no changes of VEP responses and latency in WT and naïve *Apoa1bp*$^{-/-}$ mice. $N = 15$ mice. (*F*) Total recordings of VEP responses. Left: total recordings of the VEP response of WT mice. Right: total recordings of the VEP response of naïve *Apoa1bp*$^{-/-}$ mice. (*G*) Representative images of CTB (red) labeling in the SCs of in WT and naïve *Apoa1bp*$^{-/-}$ mice. $N = 3$ mice. (*H*) Quantitative analysis of CTB fluorescence density in the SCs of WT and naïve *Apoa1bp*$^{-/-}$ mice. $N = 3$ mice. Error bars represent SEM. Statistical significance determined using one-way ANOVA or Student's *t*-test. *$P < 0.05$; **$P < 0.01$; ***$P < 0.001$; ****$P < 0.0001$. Scale bar: 100 μm (*B* and *I*); 20 μm (*D*). CNT, control; HIOP, high intraocular pressure; ns, not significant; SC, superior colliculus. (For interpretation of the references to colour in this figure legend, the reader is referred to the Web version of this article.)

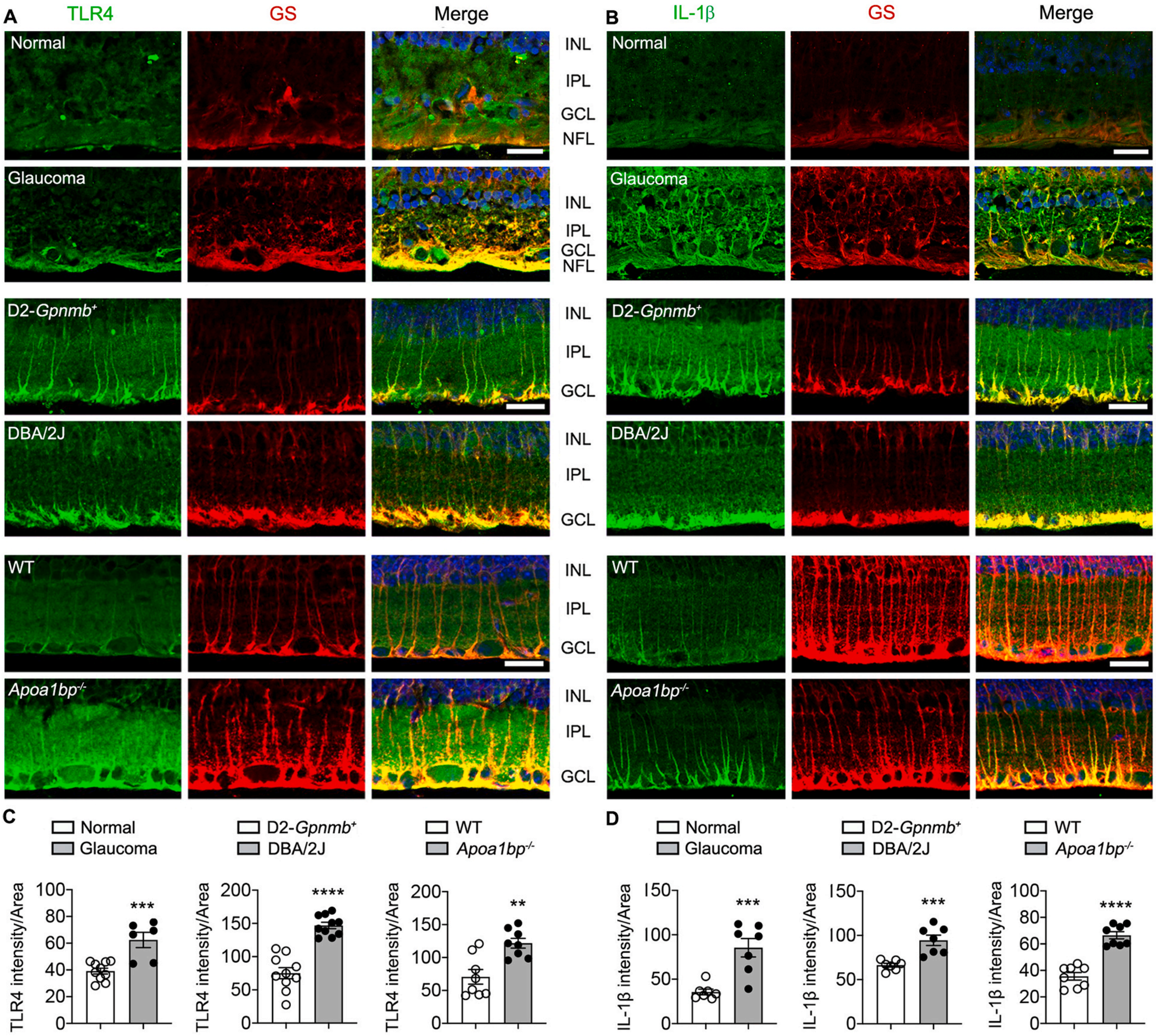

Fig. 3. Glaucomatous and *Apoa1bp*$^{-/-}$ Müller glia endfeet upregulate TLR4 and IL-1β expression. Immunohistochemical analyses for TLR4 and IL-1β were conducted on retina wax sections in glaucomatous and *Apoa1bp*$^{-/-}$ retina. (*A* and *B*) Representative images showed TLR4 and IL-1β immunoreactivities in Müller glia of the inner retinas from human patient with POAG, and glaucomatous DBA/2J and naïve *Apoa1bp*$^{-/-}$ mice. (*C* and *D*) Quantitative fluorescent intensity showed a significant increase in TLR4 and IL-1β immunoreactivities in Müller glia endfeets from human patient with POAG ($n = 5$ retina sections per group), and glaucomatous DBA/2J and naïve *Apoa1bp*$^{-/-}$ mice compared with control groups ($n = 4$ mice per group). Error bars represent SEM. Statistical significance determined using Student's *t*-test. $^{**}P < 0.01$; $^{***}P < 0.001$; $^{****}P < 0.0001$. Blue is Hoechst 33342 staining. Scale bar: 20 μm (*A* and *B*). GCL, ganglion cell layer; INL, inner nuclear layer; IPL, inner plexiform layer; NFL, nerve fiber layer. (For interpretation of the references to colour in this figure legend, the reader is referred to the Web version of this article.)

swirling membrane, were commonly seen in the *Apoa1bp*$^{-/-}$ RGC soma (Fig. 6G and H). Long extended axons distinguish RGCs from displaced amacrine cells in the GCL. Variable RGC mitochondrial structures were rendered and analyzed (Inserts in Fig. 6I and J; sMovies 3 and 4). 3D volumes showed long tubular forms of mitochondria and branched mitochondria in WT RGC somas (Fig. 6I), whereas small and rounded forms of mitochondria and sometimes branched mitochondria were observed in *Apoa1bp*$^{-/-}$ RGC somas (Fig. 6J). We also found abnormal mitochondria with vesicular inclusions and what appears to be autophagosome formation in *Apoa1bp*$^{-/-}$ RGC somas (sFig. 4C and D). Unlike in the *Apoa1bp*$^{-/-}$ Müller glia endfeet, it was verified that *Apoa1bp*$^{-/-}$ RGC mitochondria were larger (Fig. 6K, $n = 50$ mitochondria in 5 RGC soma) and occupied more of the cytoplasmic volume (Fig. 6L, $n = 10$ RGC soma) likely due to their largeness, yet they did not have increased numbers (Fig. 6M, $n = 10$ RGC soma). The form factor for mitochondria was significantly lower, indicating more rounded mitochondria caused by volume dilation in the *Apoa1bp*$^{-/-}$ RGC compared to the WT (Fig. 6N, $n = 50$ mitochondria in 5 RGC soma). As with the Müller glia endfeet, the lengths of *Apoa1bp*$^{-/-}$ mitochondria were significantly decreased in RGC somas (Fig. 6O, $n = 50$ mitochondria in 5 RGC soma); their greater volume comes from their rounding.

As implied in Fig. 6, the crista density was significantly lower in the *Apoa1bp*$^{-/-}$ RGC mitochondria (Fig. 7A, $n = 50$ mitochondria in 5 RGC soma), leading to a lower modeled rate of ATP production per mitochondrial volume (Fig. 7B). Yet, because mitochondria were larger in the *Apoa1bp*$^{-/-}$ RGC soma, each mitochondrion, on average, was modeled to produce more ATP per second (Fig. 7B). However, unlike in the *Apoa1bp*$^{-/-}$ Müller glia endfeet, the model for the rate of ATP production, which is based on 3D cristae surface area, predicts that there is not much decrease in cellular ATP production via mitochondria in the *Apoa1bp*$^{-/-}$ RGC soma (Fig. 7B, $n = 50$ mitochondria in 5 RGC soma) even though the rate of ATP production per mitochondrial volume had

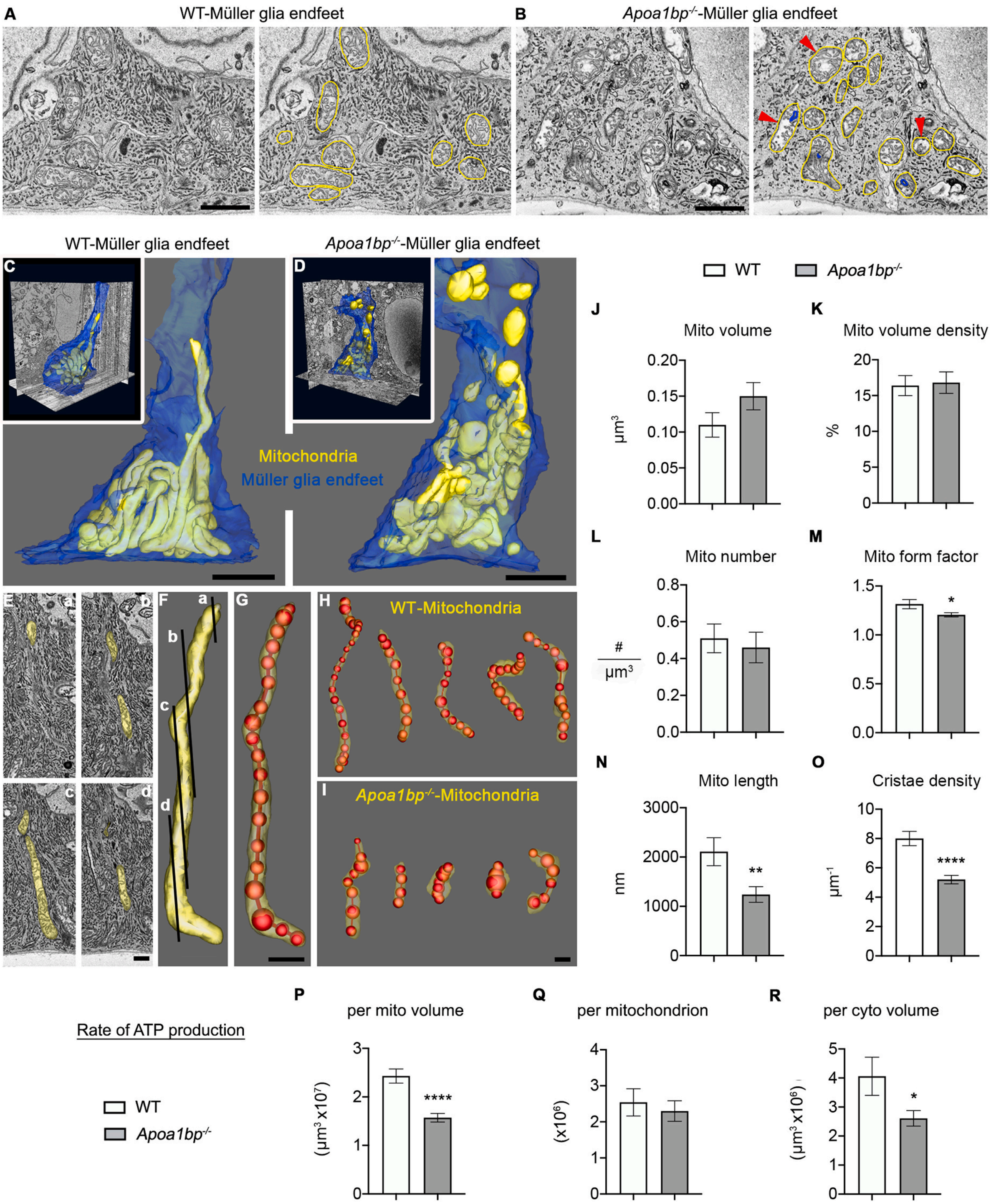

Fig. 4. AIBP deficiency induces mitochondrial fragmentation, outer membrane onion-like swirls, lower crista density, and reduces ATP production in Müller glia endfeet. (*A*) SBEM WT volume showing typical cytoplasmic structures; mitochondria (yellow trace) highlighted. (*B*) SBEM *Apoa1bp*$^{-/-}$ volume showing mitochondria (yellow trace) with lower crista density (red arrowheads) and dark outer membrane onion-like swirls (blue trace). (*C*) WT surface rendering (Volume: 4830 μm^3 30μmx23 μmx7μm; voxel size: 3nm × 3nm × 50nm) highlighting long tubular mitochondria (yellow) (cytoplasmic membrane–blue). (*D*) Surface rendering (Volume: 4408 μm^3, 29μmx19 μmx8μm; voxel size 3nm × 3nm × 50nm) showing short fragmented mitochondria (yellow) in *Apoa1bp*$^{-/-}$. (*E-G*) Expedited and accurate segmentation and analysis of mitochondria. (*E-F*) Cross image planes (a–d) showing the need for 3DEM. 357 electron micrographs (50-nm step) were serially collected to follow many mitochondria through the large volume. (*G*) Approach to determine mitochondrial length (red) and variable shapes. (*H*) Surface rendering showing long tubular forms of mitochondria in WT. (*I*) Surface rendering showing smaller, round forms of mitochondria in *Apoa1bp*$^{-/-}$. (*J*) The volume of mitochondria was not significantly different in the *Apoa1bp*$^{-/-}$. (*K*) The mitochondrial volume density in the *Apoa1bp*$^{-/-}$ was almost identical to the WT. (*L*) No significant difference in the number of mitochondria between WT and *Apoa1bp*$^{-/-}$. (*M*) The form factor for *Apoa1bp*$^{-/-}$ mitochondria was significantly lower, confirming less elongation. (*N*) The mitochondrial length was significantly lower in the *Apoa1bp*$^{-/-}$. (*O*) The crista density was significantly lower in the *Apoa1bp*$^{-/-}$. (*P*) The rate of ATP production per mitochondrial volume was lower in the *Apoa1bp*$^{-/-}$. (*Q*) The modeled rate of ATP production per mitochondrion was no different in the *Apoa1bp*$^{-/-}$. (*R*) There was a significant lowering of ATP availability per unit cellular volume in the *Apoa1bp*$^{-/-}$. *N* = 3 Müller glia from 2 mice per group. Scale bars: 1 μm (*A* and *B*), 50 nm (*C–I*). (For interpretation of the references to colour in this figure legend, the reader is referred to the Web version of this article.)

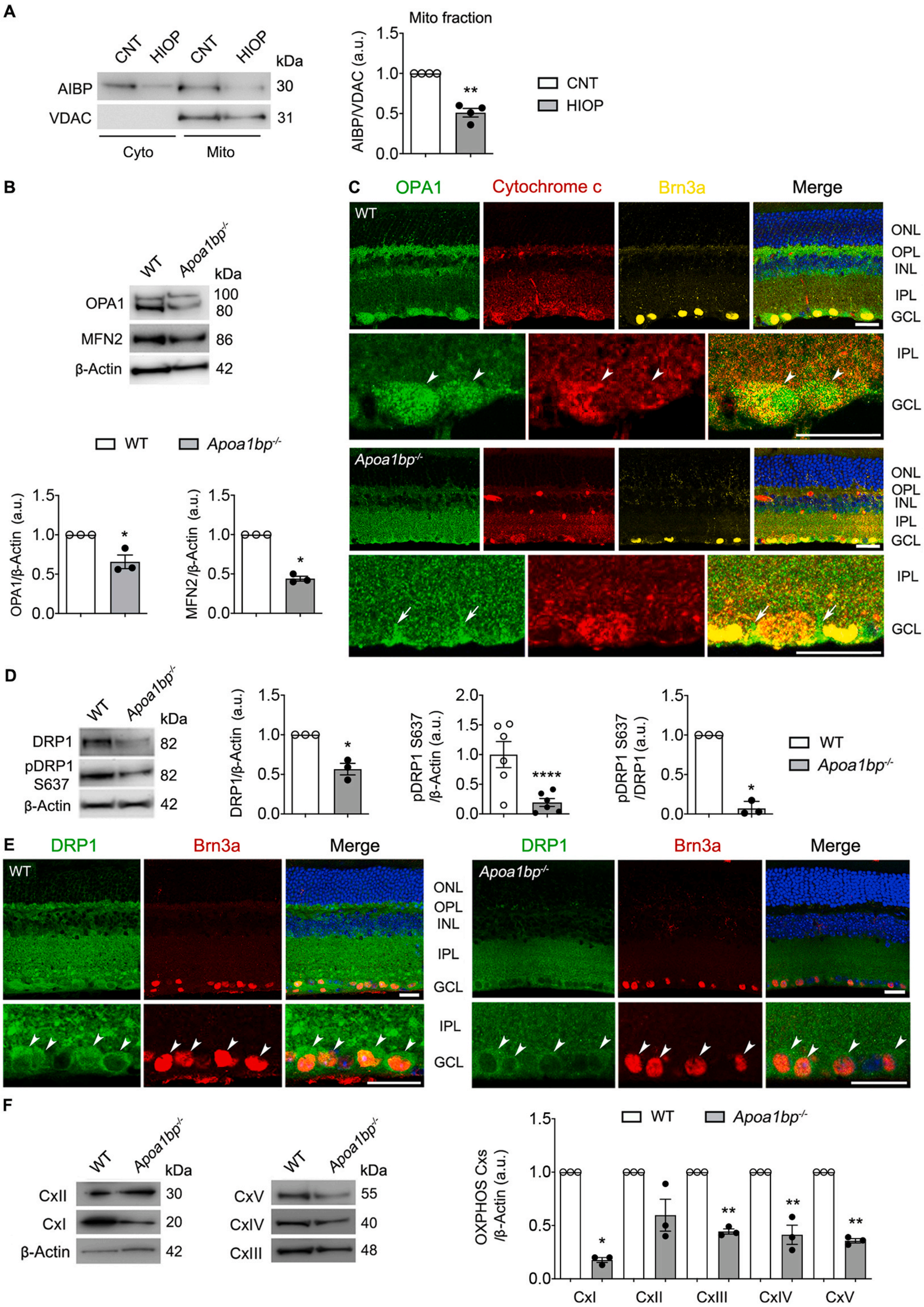

Fig. 5. AIBP deficiency impairs mitochondrial dynamics and OXPHOS activity in the retina. Mitochondrial AIBP expression was assessed in the retina of a mouse model of acute IOP elevation and alteration of mitochondrial dynamics and OXPHOS were assessed in the retina of WT and *Apoa1bp*$^{-/-}$ mice. (*A*) Using fractionation of cytosolic and mitochondrial extracts, mitochondrial AIBP protein expression in control and injured retina at 1 day after acute IOP elevation. $N = 4$ mice. (*B*) OPA1 and MFN2 protein expression in the retina of WT and *Apoa1bp*$^{-/-}$ mice. $N = 3$ mice. (*C*) Representative images showed OPA1 (green), cytochrome *c* (red) and Brn3a (yellow) immunoreactivities in the wax sections from WT and *Apoa1bp*$^{-/-}$ retinas. Arrowheads indicate accumulation of OPA1 co-labeled with cytochrome *c* in RGC somas in WT mice and arrows indicate OPA1-labeled Müller glia endfeet. $N = 3$ mice. (*D*) DRP1 and pDRP1 S637 expression in the retina of WT and *Apoa1bp*$^{-/-}$ mice. $N = 3$ mice. (*E*) Representative images showed DRP1 (green) and Brn3a (red) immunoreactivities in the wax sections from WT and *Apoa1bp*$^{-/-}$ retinas. Arrowheads indicate accumulation of DRP1 co-labeled with Brn3a in RGC somas in WT and *Apoa1bp*$^{-/-}$ mice. $N = 3$ mice. (*F*) OXPHOS Cxs protein expression in the retina of WT and *Apoa1bp*$^{-/-}$ mice. $N = 3$ mice. Error bars represent SEM. Statistical significance determined using Student's *t*-test. $^{*}P < 0.05$; $^{**}P < 0.01$; $^{****}P < 0.0001$. Blue is Hoechst 33342 staining. Scale bar: 20 μm. CNT, control; Cx, complex; GCL, ganglion cell layer; HIOP, high intraocular pressure; HP, hydrostatic pressure; INL, inner nuclear layer; IPL, inner plexiform layer; ONL, outer nuclear layer; OPL, outer plexiform layer. (For interpretation of the references to colour in this figure legend, the reader is referred to the Web version of this article.)

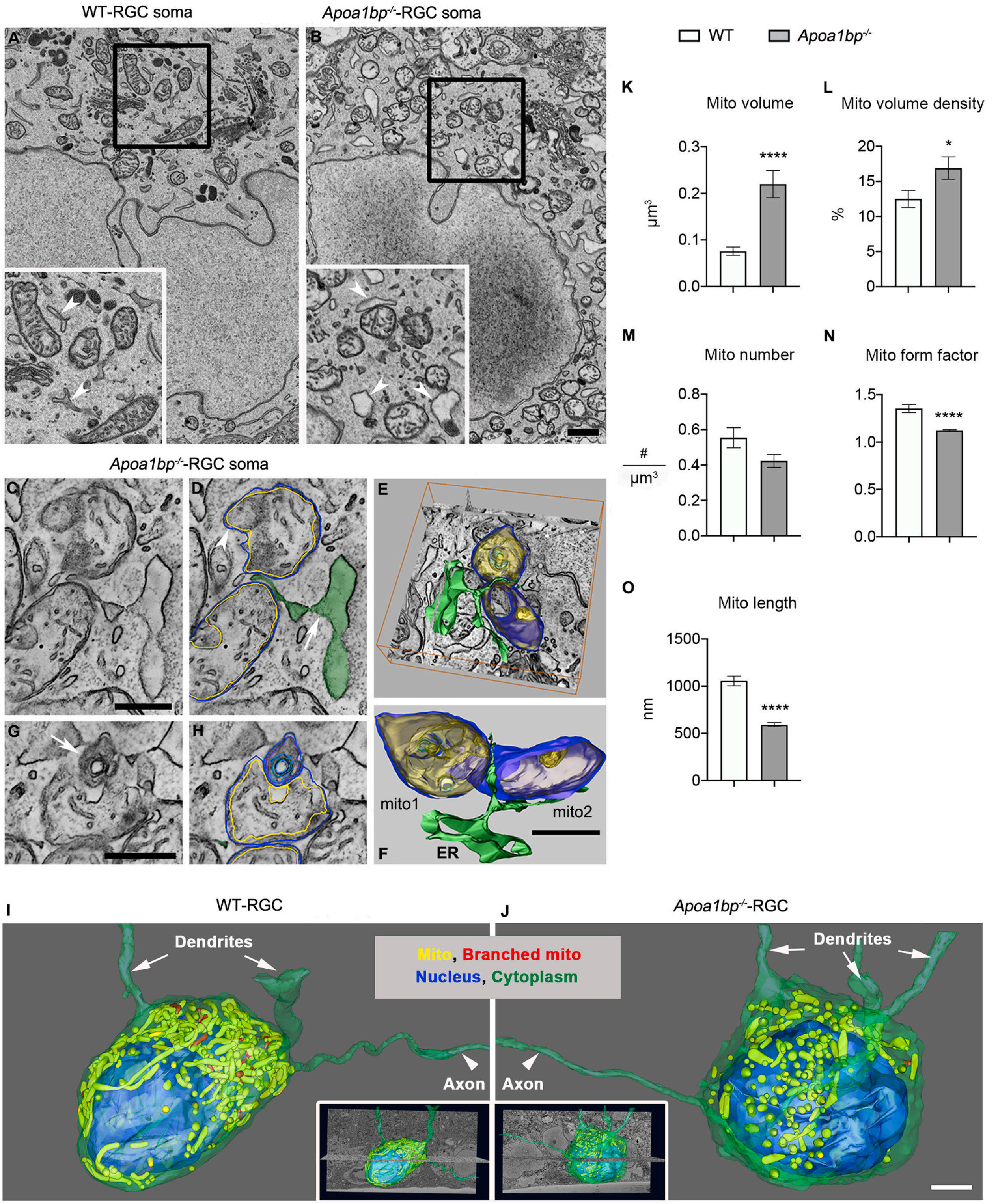

(caption on next page)

Fig. 6. AIBP deficiency triggers mitochondrial fragmentation, swelling and rounding, and ER swelling in RGC somas. (*A*) Tomographic volume of WT RGC showing typical mitochondrial and ER structures. 2xinset displays well-formed mitochondria and ER (white arrowheads). (*B*) Tomographic volume of *Apoa1bp*$^{-/-}$ RGC showing rounded mitochondria with lower crista density and swollen ER. 2xinset displays swollen ER (white arrowheads), including one contacting a mitochondrion. (*C*) *Apoa1bp*$^{-/-}$ volume showing two adjacent mitochondria and ER sandwiched at their fission site. (*D*) Mitochondrial outer membrane (blue trace), IBM (yellow trace) and ER (green fill), partly dilated (arrow). Bulge in top mitochondrion (white arrowhead) caused by expansion of both outer and IBM. Inward bulge in bottom mitochondrion (black arrowhead) caused by expansion of the IBM only. (*E*) 3D Surface-rendering overlaid on a *Apoa1bp*$^{-/-}$ volume. (*F*) Even though many ER strands are dilated, mitochondrial fission can proceed in the *Apoa1bp*$^{-/-}$. (*G*) Abnormal mitochondria with onion-like swirling membrane (white arrow) were common in the *Apoa1bp*$^{-/-}$. (*H*) Onion-like swirl (blue) not part of the IBM (yellow). (*I*) Surface rendering of SBEM sub-volume (volume: 5814 µm^3, 34µmx19 µmx9µm, voxel size:3nm × 3nm × 50nm) showing cytoplasmic membrane (green), neurites (green), nucleus (blue) long tubular form (yellow) and branched mitochondria (red) in the WT. (*J*) Surface rendering (volume: 7752 µm^3, 34µmx19 µmx12µm, voxel size: 3nm × 3nm × 50nm) showing the cytoplasmic membrane, nucleus, dendrites and axons, and smaller round form (yellow) and branched (red) mitochondria in *Apoa1bp*$^{-/-}$. (*K–O*) Measurements of structural features of mitochondria. (*K*) Volume of mitochondria was significantly greater in *Apoa1bp*$^{-/-}$. (*L*) Mitochondrial volume density was higher in Apoa1bp$^{-/-}$. (*M*) No significant difference in the number of mitochondria. (*N*) Form factor was significantly lower in the *Apoa1bp*$^{-/-}$, confirming rounded mitochondria. (*O*) Mitochondria lengths were significantly decreased in the *Apoa1bp*$^{-/-}$. *N* = 3 RGCs from 2 mice per group. Error bars represent SEM. Statistical significance determined using Student's *t*-test. *$P < 0.05$; ****$P < 0.0001$. Scale bars: 500 nm (*A-H*), 2 µm (*I-J*). (For interpretation of the references to colour in this figure legend, the reader is referred to the Web version of this article.)

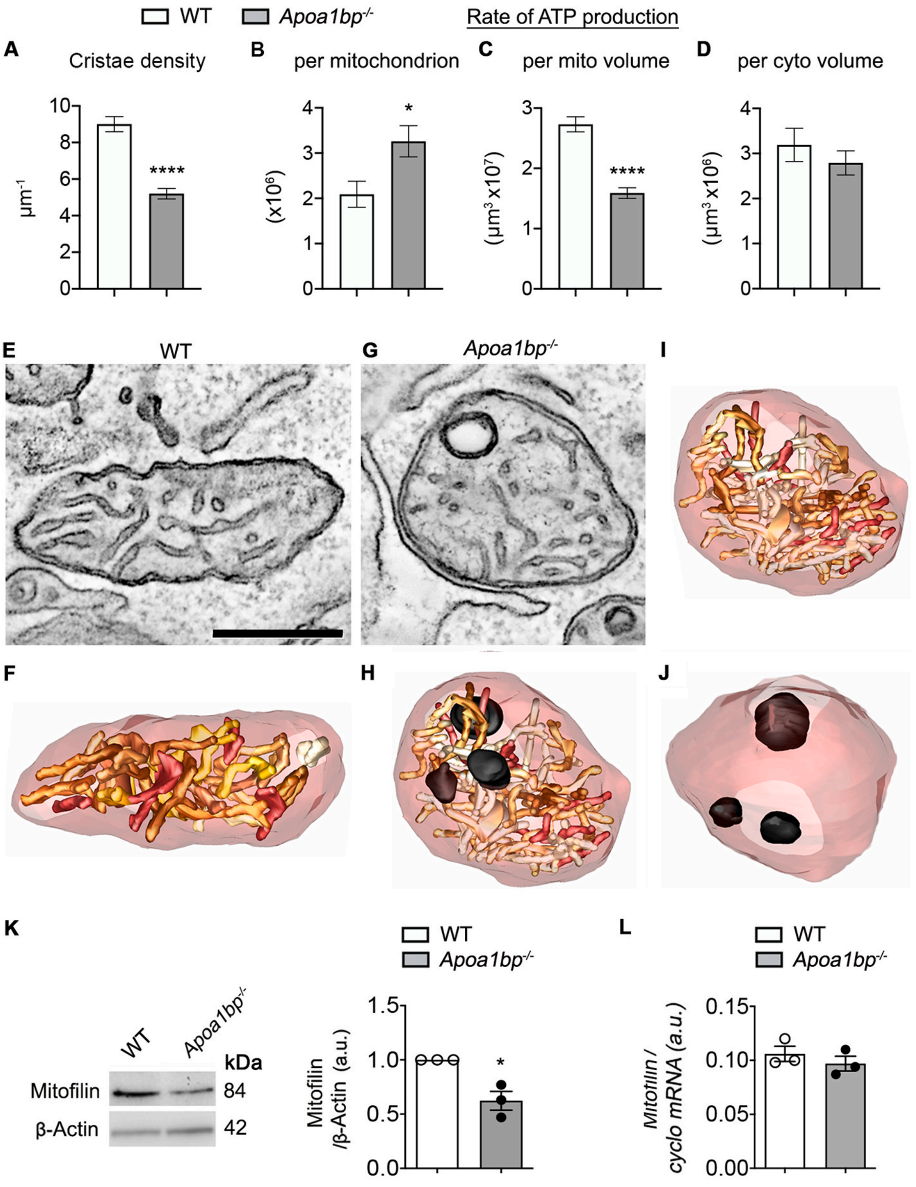

Fig. 7. AIBP deficiency reduces cristae density, ATP production and mitofilin protein expression in RGC mitochondria. (*A*) The mean crista density was significantly lower in the mitochondria of *Apoa1bp*$^{-/-}$ RGC somas. (*B*) The mean modeled rate of ATP production per mitochondrion was higher in the *Apoa1bp*$^{-/-}$ RGC soma. (*C*) The mean rate of ATP production per unit mitochondrial volume was lower in the *Apoa1bp*$^{-/-}$ RGC soma. (*D*) There was no significant lowering of modeled availability of ATP per unit cellular volume (P = 0.39). *N* = 3 RGCs from 2 mice per group. (*E-J*) The crista density was lower in the *Apoa1bp*$^{-/-}$ mitochondria due in part to onion-like outer membrane protuberances. Mitochondria-associated ER strands were often dilated. (*E*) A 4.2 nm-thick slice from a WT tomographic volume of RGC showing typical cristae. A well-formed ER strand is nearby (arrowhead). (*F*) Surface rendering of the segmented volume emphasizes the density of the cristae (shades of brown). The mitochondrial outer membrane is shown in translucent maroon. (*G*) A 4.2 nm-thick slice from an *Apoa1bp*$^{-/-}$ tomographic volume of RGC showing cristae that is less densely packed and an onion-like protuberance. An adjacent ER strand is dilated. (*H*) Surface rendering of the segmented volume emphasizes the less-dense cristae packing and the 3 protuberances (black) that occupy part of the volume that would normally have been occupied by cristae. (*I*) Surface rendering without the protuberances emphasizes the part of the volume not occupied by cristae (arrow points to one of these volumes). (*J*) Surface rendering showing only the protuberances to highlight their size relative to the mitochondrial volume. (*K*) Mitofilin protein expression was assessed by Western blot analysis in WT and *Apoa1bp*$^{-/-}$ retinas. *N* = 4 mice. (*L*) *Mitofilin* gene expression was assessed by quantitative PCR analysis in WT and *Apoa1bp*$^{-/-}$ retinas. *N* = 3 mice. Error bars represent SEM. Statistical significance determined using Student's *t*-test. *$P < 0.05$. Scale bars: 500 nm. (For interpretation of the references to colour in this figure legend, the reader is referred to the Web version of this article.)

significantly decreased (Fig. 7C, *n* = 50 mitochondria in 5 RGC soma); this decrease was simply offset by larger mitochondria. Tomographic volumes of WT RGC soma mitochondria show typical cristae (Fig. 7C and D, *n* = 10 RGC soma). In contrast, *Apoa1bp*$^{-/-}$ RGC soma mitochondria typically show cristae that are less densely packed and commonly observed onion-like protuberances. Also, adjacent ER strands are often dilated (Fig. 7E–J; sMovies 5 and 6). The crista density was lower in the *Apoa1bp*$^{-/-}$ RGC soma mitochondria due in part to these onion-like outer membrane protuberances. In summary, the *Apoa1bp*$^{-/-}$ RGC somas have mitochondria that are structurally perturbed by dilation and rounding with some localized structural perturbation of the outer membrane and some loss of cristae membrane. We next measured expression levels of mitofilin in naïve *Apoa1bp*$^{-/-}$ and WT mice. Mitofilin is a mitochondrial inner membrane protein that controls cristae architecture [48]. In the absence of AIBP, we found a significant reduction of mitofilin protein expression in the retina (Fig. 7K), suggesting that AIBP deficiency may be the underlying factor for the loss of cristae membrane. However, there was no significant difference in *mitofilin* gene expression between WT and naïve *Apoa1bp*$^{-/-}$ mice (Fig. 7L).

3.7. AIBP deficiency induces oxidative stress and MAPK signaling activation in RGCs

Under oxidative stress conditions, sirtuin 3 (SIRT3) impairment reduces the activity of superoxide dismutase 2 (SOD2) and increases ROS production [49,50], and multiple mitogen-activated protein kinases (MAPKs) signaling pathways such as p38 and extracellular signal-regulated kinase 1/2 (ERK1/2) are activated [51,52]. Thus, we tested whether AIBP regulates expression levels of SIRT3 and SOD2, as well as p38 and ERK1/2 activation in WT and naïve Apoa1bp$^{-/-}$ mice. In the absence of AIBP, we found that SIRT3 and SOD2 protein expression were significantly decreased in the retina (Fig. 8A and B). However, there were no statistically significant differences in Sirt3 and Sod2 gene expression (sFig. 3B). Also, we found that SIRT3 and SOD2 immunoreactivity was dramatically diminished in the IPL and GCL, especially in the in Brn3a-positive RGCs (Fig. 8C and D). Next, we found that AIBP deficiency significantly increased phosphorylation of p38 and ERK1/2 in the retina (Fig. 8E and F). Consistently, we also observed that phospho-p38 and phospho-ERK1/2 immunoreactivities were increased in the inner retinal layer in naïve *Apoa1bp*$^{-/-}$ mice (Fig. 8G and H). We noted that AIBP deficiency showed an increased pattern of phospho-p38 immunoreactivity in Brn3a-positive RGCs (Fig. 8G and H).

3.8. Administration of AIBP promotes RGC survival and inhibits inflammatory responses in IOP mouse model

Since AIBP deficiency was associated with a neuroinflammatory and RGC death phenotype, next we tested the hypothesis that injections of recombinant AIBP will be protective. We intravitreally injected recombinant AIBP protein or BSA (1 μL, 0.5 mg/ml) into C57BL/6J mice at 2 days before the induction of acute IOP elevation as described above. At 24 h after IOP elevation, we performed TUNEL staining and RBPMS immunohistochemistry. In BSA-injected animals, elevated IOP significantly increased the number of TUNEL-positive cells in all retinal layers compared with control mice (Fig. 9A and B). In the GCL, RBPMS-positive RGCs were co-stained with TUNEL, indicating apoptotic RGC death. In contrast, we remarkably observed that AIBP treatment significantly reduced the number of TUNEL-positive cells in the retina in response to elevated IOP, whereas there were no TUNEL-positive cells in both sham controls (BSA and AIBP) (Fig. 9A and B). To determine the effect of AIBP administration on inflammatory responses in activated Müller glia in response to elevated IOP, we quantified expression levels of IL-1β protein in Müller glia endfeet by measuring relative fluorescence intensity of IL-1β immunoreactivity in the GCL. Consistent with the data from glaucomatous retinas (Fig. 3), we found that elevated IOP significantly increased IL-1β immunoreactivity in the endfeet of Müller glia of BSA-treated control retina compared with BSA-treated sham control (Fig. 9C and D). In AIBP-treated animals, however, we found that IL-1β immunoreactivity was significantly decreased in the endfeet of Müller glia against elevated IOP (Fig. 9C and D). There was no significant difference in IL-1β immunoreactivity between BSA- and AIBP-treated sham control groups (Fig. 9C and D).

4. Discussion

Factors contributing to neuroinflammation, the process that plays a critical role in glaucomatous neurodegeneration, are poorly understood. In the present study, we identified AIBP as an important neuroprotective protein in the retina. We demonstrated that elevated IOP reduced AIBP expression in glaucomatous retina and that *Apoa1bp*$^{-/-}$ Müller glia had an upregulated TLR4-mediated inflammatory response via increasing IL-1β expression that is accompanied by compromised mitochondrial dynamics and energy depletion. In parallel, we found that ABIP deficiency contributed to dysfunctional RGC mitochondria, oxidative stress and visual dysfunction. Also, AIBP deficiency exacerbated RGC death in response to elevated IOP. Remarkably, recombinant AIBP administration prevented apoptotic RGC cell death and inflammatory responses in Müller glia *in vivo*. Here we propose for the first time that AIBP could be a therapeutic target for treating neuroinflammation, mitochondrial dysfunction and RGC death in glaucoma progression.

AIBP has been known to accelerate cholesterol efflux from endothelial cells and macrophages [4,7–9,23,41]. Accumulating evidence indicates that cholesterol is considered as a risk factor for POAG [53–57]. Indeed, epidemiological studies indicate that POAG is linked to single-nucleotide polymorphisms of ABCA1 [53–55]. Interestingly, ABCA1 is expressed in human RGCs [53,54], which is significantly decreased in RGCs in response to elevated IOP [58]. In the current study, both AIBP and ABCA1 protein expression were found to be reduced in glaucomatous retina. A previous study has demonstrated that AIBP mediates the stabilization of ABCA1 by facilitating apoA-1 binding to ABCA1 and prevents ABCA1 degradation via the ubiquitination pathway [41]. Although the relationship between AIBP and ABCA1, particularly in RGCs needs to be elucidated, it is likely that AIBP stabilizes ABCA1 and regulates cholesterol efflux in glaucomatous RGCs. Moreover, loss of AIBP induced by elevated IOP may contribute to deregulation of ABCA1 in glaucomatous neurodegeneration.

Epidemiological studies indicate that human POAG is linked to single-nucleotide polymorphisms of TLR4 [43,45] and recent evidence from animal studies further suggests that TLR4-dependent signaling is an important factor in the pathogenesis of POAG [14,44]. In the current study, we found that glaucomatous retina significantly increased *Tlr4* gene expression. Moreover, both glaucomatous and *Apoa1bp*$^{-/-}$ Müller glia endfeet, which are in close contact with RGCs, were characterized by increased TLR4 protein expression. Under normal conditions, Müller glia interact with and help maintain neurons including RGCs, but reactive Müller glia contribute to neuronal degeneration [59]. Since RGC is a main affected cell type in glaucomatous neurodegeneration, it is likely that increased immunoreactivity of GS and TLR4 in the endfeet of Müller glia in glaucomatous and *Apoa1bp*$^{-/-}$ retinas are associated with degenerative or vulnerable RGCs. Since our previous study demonstrated that AIBP bound to activated microglia via TLR4, augmented cholesterol efflux and also the disruption of lipid rafts in LPS-stimulated cells, as well as reduced TLR4 dimerization [7,11], the current results strongly suggest that AIBP mediates inhibition of TLR4 activity in Müller glia and may have a critical role in protection against glaucomatous neuroinflammation. Recent evidence suggests that acute IOP elevation induces TLR4-mediated inflammasome activation, including pyrin domain containing 1 (NLRP1) and NLRP3, and activates the IL-1β cascade in the retina [14,15]. Further, genetic deletion or pharmacological inhibition of TLR4 significantly reduces RGC death and proinflammatory responses in experimental glaucoma [44,60,61]. Thus, we propose that loss of AIBP and activation of TLR4 signaling in glaucomatous Müller glia are critical to inflammatory response-mediated glaucomatous RGC degeneration. Indeed, this notion is strongly supported by our results that show a significant increase in IL-1β protein expression in both glaucomatous and *Apoa1bp*$^{-/-}$ Müller glia endfeet.

In transfected cells, AIBP was localized to mitochondria [22], but the role of AIBP in regulation of mitochondrial structure and function in mammalian cells remained unknown. Interestingly, activated TLR4

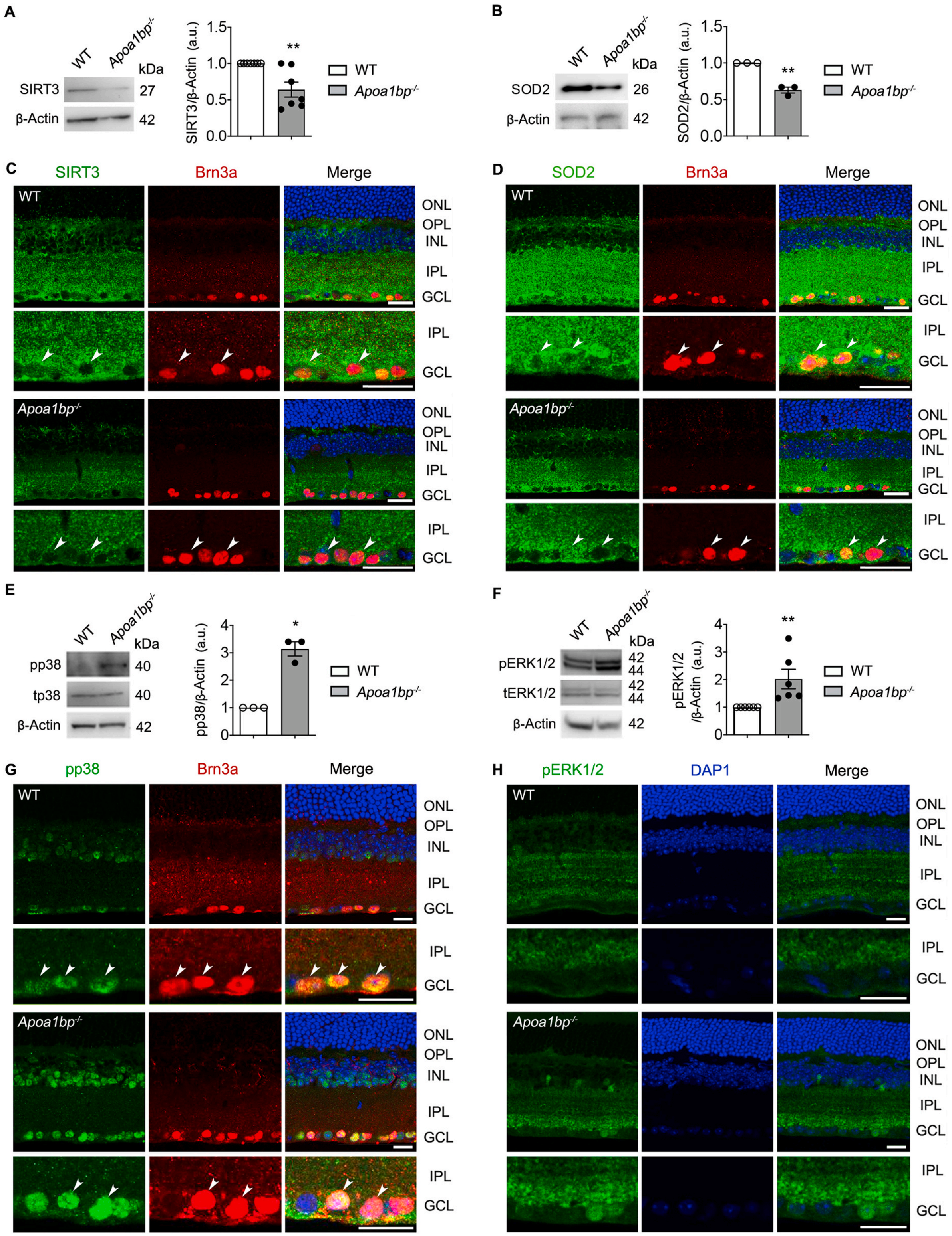

Fig. 8. AIBP deficiency induces oxidative stress and activates MAPK signaling in the retina. Oxidative stress and MAPKs signaling were assessed in the retina of WT and *Apoa1bp*$^{-/-}$ mice. (*A* and *B*) SIRT3 and SOD2 protein expression in the retina of WT and *Apoa1bp*$^{-/-}$ mice. *N* = 3–7 mice. (*C* and *D*) Representative images showed SIRT3 (green), SOD2 (green) and Brn3a (red) immunoreactivities in the wax sections from WT and *Apoa1bp*$^{-/-}$ retinas. Arrowheads indicate accumulation of SIRT3 or SOD2 co-labeled with Brn3a in RGC somas in WT and *Apoa1bp*$^{-/-}$ mice. *N* = 3 mice. (*E* and *F*) Phospho-p38 (pp38) and phospho-ERK1/2 (pERK1/2) protein expression in the retina of WT and *Apoa1bp*$^{-/-}$ mice. *N* = 3–6 mice. (*G* and *H*) Representative images showed pp38 (green), pERK1/2 (green) and Brn3a (red) immunoreactivities in WT and *Apoa1bp*$^{-/-}$ retinas. Arrowheads indicate accumulation of phospho-p38 co-labeled with Brn3a in RGC somas in WT and *Apoa1bp*$^{-/-}$ mice. *N* = 3 mice. Error bars represent SEM. Statistical significance determined using Student's *t*-test. $^*P < 0.05$; $^{**}P < 0.01$. Blue is Hoechst 33342 staining. Scale bar: 20 μm. GCL, ganglion cell layer; INL, inner nuclear layer; IPL, inner plexiform layer; ONL, outer nuclear layer; OPL, outer plexiform layer. (For interpretation of the references to colour in this figure legend, the reader is referred to the Web version of this article.)

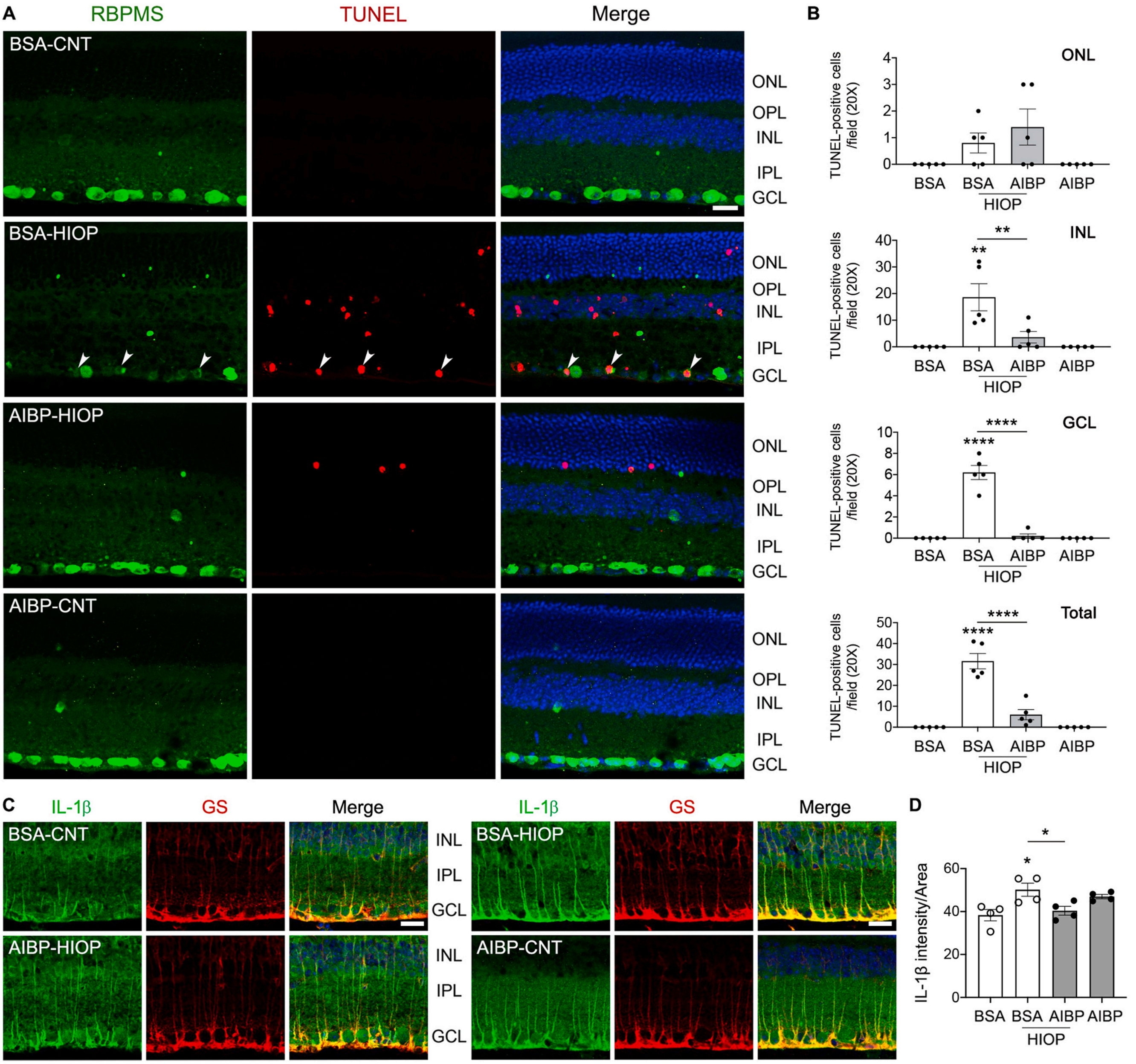

Fig. 9. AIBP promotes RGC survival and prevents glia-mediated inflammatory responses against elevated pressure. Apoptotic cell death was assessed in a mouse model of acute IOP elevation, and IL-1β immunoreactivity was assessed in retinal Müller glia. (*A* and *B*) Recombinant AIBP protein or BSA (1 μL, 0.5 mg/ml) was intravitreally injected at 2 days before acute IOP elevation and assessed TUNEL-positive cells in the retina of WT mice at 1 day after acute IOP elevation. Following RBPMS (green) immunohistochemistry, TUNEL (red) staining was conducted. (*A*) Representative images showed RBPMS-positive RGCs in the GCL and TUNEL-positive cells in the retinas. (*B*) Quantitative analysis by TUNEL-positive cell counting. $N = 5$ mice. (*C*) Representative images showed IL-1β immunoreactivity in the inner retina. (*D*) Quantitative analyses for fluorescent intensity showed that AIBP treatment significantly decreased in IL-1β immunoreactivity in Müller glia endfeets against elevated IOP. $n = 4$ mice. Error bars represent SEM. Statistical significance determined using one-way ANOVA or Student's *t*-test. $^{*}P < 0.05$; $^{**}P < 0.01$; $^{***}P < 0.001$; $^{****}P < 0.0001$. Blue is Hoechst 33342 staining. Scale bar: 20 μm. BSA, bovine serum albumin; CNT, control; GCL, ganglion cell layer; EHP, elevated hydrostatic pressure; HIOP, high intraocular pressure; INL, inner nuclear layer; IPL, inner plexiform layer; NP, no pressure; ONL, outer nuclear layer; OPL, outer plexiform layer. (For interpretation of the references to colour in this figure legend, the reader is referred to the Web version of this article.)

signaling is associated with mitochondrial damage in microglia caused by intracellular ROS and defective mitochondrial dynamics [20,21]. In the current study, we demonstrated for the first time that the loss of AIBP impaired mitochondrial network and function in Müller glia endfeet via induction of mitochondrial fragmentation and reduction of ATP production. Recent evidence suggests that Müller glia-induced neuroinflammation is linked with RGC death [62] and that Müller glia-mediated lactate is a critical source in maintaining RGC energy metabolism and survival [32]. Given our findings and those of others, it is conceivable that loss of AIBP augments the TLR4 signaling in glaucomatous Müller glia that might compromise mitochondrial network, increase ROS production and deplete energy production, leading to dysfunction of Müller glia, activation of inflammatory responses and RGC death.

Another possible mechanism of a protective role of AIBP in glaucoma is related to angiogenesis. Müller glia are associated with the regulation of angiogenesis that is linked to a severe form of secondary glaucoma commonly associated with proliferative diabetic retinopathy, ischemic central retinal vein occlusion, and ocular ischemic syndrome [63]. Further, Müller glia activation is increased with age in glaucomatous

DBA/2J mice, showing abnormal neovascularization [64]. Since previous studies have demonstrated that loss of AIBP results in dysregulated sprouting/branching angiogenesis and that enhanced AIBP expression inhibits angiogenesis [4,8], it is possible that Müller glia dysfunction induced by loss of AIBP may contribute to abnormal angiogenesis in secondary glaucoma. In addition, microglial activation is a common inflammatory response to elevated IOP-induced retinal injury and microglia-mediated TLR4 activation is involved in retinal degeneration [14,65]. Given that elevated IOP increased *Tlr4* gene expression in the retina and augmented microglial activation in Ap*oa1bp*$^{-/-}$ retina, our findings collectively suggest the possibility that loss of AIBP exacerbates vulnerability to elevated IOP-induced RGC death through TLR4 signaling activation, mitochondrial dysfunction and inflammatory response by activated Müller glia and microglia.

We also provide the first evidence that AIBP regulates structural and functional integrity of mitochondria in RGCs. Our study intriguingly demonstrated a significant loss of mitochondrial AIBP in the retina in response to elevated IOP. Moreover, loss of AIBP significantly impaired not only the OXPHOS system in the retina but also mitochondrial dynamics and ATP production in RGCs, resulting in extensive mitochondrial fragmentation, energy depletion and possible autophagosome formation. Since we have demonstrated that impairment of mitochondrial dynamics and function was strongly linked to RGC death in glaucomatous neurodegeneration [16,19,25,66–68], it is likely that AIBP might play a critical role in mitochondrial quality control to maintain cellular homeostasis by preserving mitochondrial dynamics and bioenergetics in RGCs against glaucomatous insults such as elevated IOP and oxidative stress. Since degenerative pruning of RGC dendrites and their dysfunctional synapse, as well as mitochondrial degeneration have been implicated as early features of glaucomatous neurodegeneration [69,70], combined, these and our results with decreased AIBP in the inner retina and Müller glia activation suggest an intriguing possibility that loss of AIBP in the inner retina may affect not only RGC soma and axon in the GCL, but also RGC dendrites and their synapses in the IPL in an autocrine/paracrine manner during glaucomatous neurodegeneration.

SIRT3, a mitochondrial NAD^{+}-dependent deacetylase, has protective roles against oxidative stress, neuroinflammation and neurodegeneration [71,72]. SIRT3-mediated SOD2 activation and deacetylation reduces ROS levels, leading to the enhancement of resistance against oxidative stress [73,74]. Our study demonstrated that loss of AIBP significantly reduced the expression levels of SIRT3 and SOD2 proteins in the inner retina including RGCs. Recent evidence indicates that the SIRT3-SOD2 pathway is linked to inflammation and oxidative stress [75,76]. In line with these and our findings, it is possible that mitochondrial AIBP may contribute to the stabilization of the SIRT3-SOD2 axis, rescuing RGC mitochondria from neuroinflammation and/or oxidative stress. As shown in Fig. 8, SIRT3 and SOD2 are widely expressed in the retina, consistent with previous studies [19,77,78], and AIBP may contribute to SIRT3-SOD2-mediated protection of retinal structure and cells against oxidative stress. Under oxidative stress conditions, multiple MAPK signaling pathways, including p38 and ERK1/2, are activated [51,52]. Our study demonstrated that loss of AIBP persistently increased phosphorylation of p38 and ERK1/2 in the retina. p38 is phosphorylated in response to cytokines and oxidative stress [79, 80] and activation of the p38 signaling pathway leads to mitochondrial dysfunction and inflammatory responses [81–84]. Because a p38 inhibitor blocks mitochondrial dysfunction and inhibits cytochrome *c* release [85], it is likely that retinal AIBP not only plays a role in the stabilization of mitochondrial proteins, but also inhibits stress-activated intracellular signaling responses, such as p38 activation. On the other hand, ERK1/2 is also activated in response to cytokines, free radicals and inflammatory factors in neurodegenerative diseases [86,87]. In experimental glaucoma, ERK1/2 activation has a neuroprotective effect on RGC survival [88–91]. Since phosphorylation of p38 and ERK1/2 induced by lipopolysaccharide (LPS) in alveolar macrophages is inhibited in the presence of AIBP [9], our study suggests that AIBP may contribute to a differential regulation of MAPK signaling pathways in RGCs against inflammatory responses and/or oxidative stress.

Our recent studies have demonstrated that recombinant AIBP protein administration reduced not only spinal myeloid cell lipid rafts, TLR4 dimerization, neuroinflammation, and glial activation in facilitated pain states, but also LPS-induced airspace neutrophilia, alveolar capillary leak, and secretion of IL-6 in acute lung inflammation [9,11]. These results demonstrated a mechanism by which AIBP regulates neuroinflammation and suggested the therapeutic potential of AIBP in treating preexisting pain states and lung inflammation. In the current study, we found that intravitreal administration of AIBP significantly protected not only RGCs in the GCL but also cells in the INL against apoptotic cell death, and reduced IL-1β-mediated inflammatory responses in Müller glia in response to elevated IOP. Müller glia are widely distributed throughout the entire retina in which their endfeet resides in the GCL and cell body sits in the INL [92]. Interestingly, it has been reported that TLR4-mediated neuroinflammation was highly associated with apoptotic cell death in the INL and GCL of the ischemic retina, and that inhibition of TLR4 signaling activation blocked apoptosis in the retinal layers, INL and GCL [15]. Based on these and current finding, it is possible that AIBP deficiency may increase susceptibility in not only RGCs but also Müller glia in response to elevated IOP. Thus, we propose that AIBP may have a therapeutic potential for treating glaucoma via blocking glia-driven neuroinflammation.

In addition, accumulating evidence suggests that damage-associated molecular patterns (DAMPs) which are endogenous activators of TLR4 released by damaged cells activate microglia and produce inflammatory cytokines [10,93]. The activated microglia-mediated neuroinflammation is an early event in glaucoma, leading to Müller glia activation, neuronal damage, and RGC loss [94,95]. Bidirectional interaction between activated microglia and Müller glia in the retinal-injured model induces adaptive responses. Cross-talk between Müller glia and activated microglia increases pro-inflammatory cytokine production which in turn facilitates further activation of microglia in a positive feedback loop and Müller glia-microglia adhesion via upregulation of adhesion molecules [96]. Thus, understanding of potential effect of AIBP on bidirectional signaling between Müller glia and activated microglial may help to limit further amplifying inflammatory signaling and RGC death, and highlight therapeutic strategies for neuroinflammatory glaucoma. Further studies will determine whether administration of AIBP also preserves RGC and glia mitochondria and whether this mechanism contributes to RGC survival and preservation of glial function against glaucomatous insults.

5. Conclusion

In summary, our study connects for the first time AIBP with protecting mechanisms controlling mitochondrial pathogenic mechanisms, neuroinflammation and RGC death as illustrated in the graphical abstract. Here, we propose that combined therapeutic strategies that block glia-driven inflammatory TLR4/IL-1β axis and mitochondrial dysfunction in glaucomatous neurodegeneration are likely to be beneficial. Further studies aimed at identifying the AIBP target pathological pathways and understanding the potential mechanisms of AIBP-mediated neuroprotection may lead to developing a new therapeutic approach for glaucoma and other inflammatory conditions.

Author contributions

S.H. Choi, K.Y. Kim, G.A.P, Y.I. Miller, and W.K. Ju designed research. S.H. Choi, K.Y. Kim, G.A. Perkins, S. Phan, G. Edwards, Y. Xia, J. Kim, and W.K. Ju performed research. S.H. Choi, K.Y. Kim, G.A. Perkins, S. Phan, G. Edwards, J. Kim, D. Skowronska-Krawczyk, and W. K. Ju analyzed data. S.H. Choi, K.Y. Kim, G.A. Perkins, R.N. Weinreb, M. H. Ellisman, Y.I. Miller, and W.K. Ju wrote and revised the paper.

Funding

This work was supported in part by National Institutes of Health grant EY018658 and UCSD Academic Senate to WKJ, National Institutes of Health grants HL135737, HL136275 and NS102432 to YIM, National Institutes of Health grant EY027011 and RPB Special Scholar Award to DSK, National Institutes of Health grants P30 EY022589 and T32 EY026590, and National Institutes of Health grant P41GM103412 to MHE.

Declaration of competing interest

W.K. Ju, S.H. Choi, and Y.I. Miller are co-inventors named on patents and patent applications by the University of California, San Diego. Y.I. Miller is a scientific co-founder of Raft Pharmaceuticals LLC. The terms of this arrangement have been reviewed and approved by the University of California, San Diego in accordance with its conflict of interest policies. The other authors declare that they have no conflict of interest.

Acknowledgements

We would like to acknowledge a kind gift of a rabbit polyclonal anti-AIBP antibody from Dr. Longhou Fang (Houston Methodist Research Institute).

Appendix A. Supplementary data

Supplementary data to this article can be found online at https://doi.org/10.1016/j.redox.2020.101703.

References

[1] H. Chen, et al., Commensal microflora-induced T cell responses mediate progressive neurodegeneration in glaucoma, Nat. Commun. 9 (2018) 3209.

[2] P.A. Williams, N. Marsh-Armstrong, G.R. Howell, I.I.o.A. Lasker, P. Glaucomatous Neurodegeneration, Neuroinflammation in glaucoma: a new opportunity, Exp. Eye Res. 157 (2017) 20–27.

[3] M. Ritter, et al., Cloning and characterization of a novel apolipoprotein A-I binding protein, AI-BP, secreted by cells of the kidney proximal tubules in response to HDL or ApoA-I, Genomics 79 (2002) 693–702.

[4] L. Fang, et al., Control of angiogenesis by AIBP-mediated cholesterol efflux, Nature 498 (2013) 118–122.

[5] A.Y. Marbaix, et al., Extremely conserved ATP- or ADP-dependent enzymatic system for nicotinamide nucleotide repair, J. Biol. Chem. 286 (2011) 41246–41252.

[6] I.A. Shumilin, et al., Identification of unknown protein function using metabolite cocktail screening, Structure 20 (2012) 1715–1725.

[7] L. Fang, Y.I. Miller, Regulation of lipid rafts, angiogenesis and inflammation by AIBP, Curr. Opin. Lipidol. 30 (2019) 218–223.

[8] R. Mao, et al., AIBP limits angiogenesis through gamma-secretase-mediated upregulation of notch signaling, Circ. Res. 120 (2017) 1727–1739.

[9] S.H. Choi, et al., AIBP augments cholesterol efflux from alveolar macrophages to surfactant and reduces acute lung inflammation, JCI Insight 3 (2018).

[10] Y.I. Miller, J.M. Navia-Pelaez, M. Corr, T.L. Yaksh, Lipid rafts in glial cells: Role in neuroinflammation and pain processing, J. Lipid Res. 61 (2020) 655–666.

[11] S.A. Woller, et al., Inhibition of neuroinflammation by AIBP: Spinal effects upon facilitated pain states, Cell Rep. 23 (2018) 2667–2677.

[12] A.R. Tall, L. Yvan-Charvet, Cholesterol, inflammation and innate immunity, Nat. Rev. Immunol. 15 (2015) 104–116.

[13] X. Zhu, et al., Macrophage ABCA1 reduces MyD88-dependent Toll-like receptor trafficking to lipid rafts by reduction of lipid raft cholesterol, J. Lipid Res. 51 (2010) 3196–3206.

[14] W. Chi, et al., Caspase-8 promotes NLRP1/NLRP3 inflammasome activation and IL-1 beta production in acute glaucoma, Proc. Natl. Acad. Sci. U. S. A. 111 (2014) 11181–11186.

[15] Y. Qi, et al., Retinal ischemia/reperfusion injury is mediated by Toll-like receptor 4 activation of NLRP3 inflammasomes, Invest. Ophthalmol. Vis. Sci. 55 (2014) 5466–5475.

[16] K.Y. Kim, et al., DRP1 inhibition rescues retinal ganglion cells and their axons by preserving mitochondrial integrity in a mouse model of glaucoma, Cell Death Dis. 6 (2015) e1839.

[17] P.A. Williams, et al., Vitamin B3 modulates mitochondrial vulnerability and prevents glaucoma in aged mice, Science 355 (2017) 756–760.

[18] M. Harun-Or-Rashid, et al., Structural and functional rescue of chronic metabolically stressed optic nerves through respiration, J. Neurosci. 38 (2018) 5122–5139.

[19] G. Edwards, et al., Loss of AKAP1 triggers Drp1 dephosphorylation-mediated mitochondrial fission and loss in retinal ganglion cells, Cell Death Dis. 11 (2020) 254.

[20] G. Feng, et al., LPS enhances platelets aggregation via TLR4, which is related to mitochondria damage caused by intracellular ROS, but not extracellular ROS, Cell. Immunol. 328 (2018) 86–92.

[21] S.Y. Kim, et al., Isorhamnetin alleviates lipopolysaccharide-induced inflammatory responses in BV2 microglia by inactivating NF-kappaB, blocking the TLR4 pathway and reducing ROS generation, Int. J. Mol. Med. 43 (2019) 682–692.

[22] A.Y. Marbaix, et al., Occurrence and subcellular distribution of the NADPHX repair system in mammals, Biochem. J. 460 (2014) 49–58.

[23] D.A. Schneider, et al., AIBP protects against metabolic abnormalities and atherosclerosis, J. Lipid Res. 59 (2018) 854–863.

[24] W.K. Ju, K.Y. Kim, Measuring glutamate receptor activation-induced apoptotic cell death in ischemic rat retina using the TUNEL assay, Methods Mol. Biol. 740 (2011) 149–156.

[25] W.K. Ju, et al., Intraocular pressure elevation induces mitochondrial fission and triggers OPA1 release in glaucomatous optic nerve, Invest. Ophthalmol. Vis. Sci. 49 (2008) 4903–4911.

[26] G.R. Howell, et al., Axons of retinal ganglion cells are insulted in the optic nerve early in DBA/2J glaucoma, J. Cell Biol. 179 (2007) 1523–1537.

[27] D.M. Inman, R.M. Sappington, P.J. Horner, D.J. Calkins, Quantitative correlation of optic nerve pathology with ocular pressure and corneal thickness in the DBA/2 mouse model of glaucoma, Invest. Ophthalmol. Vis. Sci. 47 (2006) 986–996.

[28] W.K. Ju, et al., Selective neuronal survival and upregulation of PCNA in the rat inner retina following transient ischemia, J. Neuropathol. Exp. Neurol. 59 (2000) 241–250.

[29] D. Lee, et al., Coenzyme Q10 ameliorates oxidative stress and prevents mitochondrial alteration in ischemic retinal injury, Apoptosis 19 (2014) 603–614.

[30] G. Perkins, et al., Electron tomography of neuronal mitochondria: Three-dimensional structure and organization of cristae and membrane contacts, J. Struct. Biol. 119 (1997) 260–272.

[31] D.H. Song, et al., Biophysical significance of the inner mitochondrial membrane structure on the electrochemical potential of mitochondria, Phys. Rev. E - Stat. Nonlinear Soft Matter Phys. 88 (2013), 062723.

[32] R. Vohra, M. Kolko, Lactate: more than merely a metabolic waste product in the inner retina, Mol. Neurobiol. 57 (2020) 2021–2037.

[33] G.C. Garcia, et al., Mitochondrial morphology provides a mechanism for energy buffering at synapses, Sci. Rep. 9 (2019) 18306.

[34] D. Attwell, S.B. Laughlin, An energy budget for signaling in the grey matter of the brain, J. Cerebr. Blood Flow Metabol. 21 (2001) 1133–1145.

[35] G.T. Prusky, N.M. Alam, S. Beekman, R.M. Douglas, Rapid quantification of adult and developing mouse spatial vision using a virtual optomotor system, Invest. Ophthalmol. Vis. Sci. 45 (2004) 4611–4616.

[36] W.H. Ridder 3rd, S. Nusinowitz, The visual evoked potential in the mouse–origins and response characteristics, Vis. Res. 46 (2006) 902–913.

[37] L.R. Rocha, et al., Early removal of senescent cells protects retinal ganglion cells loss in experimental ocular hypertension, Aging Cell 19 (2020), e13089.

[38] W. Liu, et al., Neuronal Epac1 mediates retinal neurodegeneration in mouse models of ocular hypertension, J. Exp. Med. 217 (2020).

[39] S.W. John, et al., Essential iris atrophy, pigment dispersion, and glaucoma in DBA/2J mice, Invest. Ophthalmol. Vis. Sci. 39 (1998) 951–962.

[40] R.T. Libby, et al., Susceptibility to neurodegeneration in a glaucoma is modified by Bax gene dosage, PLoS Genet. 1 (2005) 17–26.

[41] M. Zhang, et al., Apolipoprotein A-1 binding protein promotes macrophage cholesterol efflux by facilitating apolipoprotein A-1 binding to ABCA1 and preventing ABCA1 degradation, Atherosclerosis 248 (2016) 149–159.

[42] F.K. Horn, et al., Monitoring glaucoma progression with visual evoked potentials of the blue-sensitive pathway, Invest. Ophthalmol. Vis. Sci. 43 (2002) 1828–1834.

[43] J. Navarro-Partida, et al., Association of Toll-like receptor 4 single-nucleotide polymorphisms Asp299Gly and Thr399Ile with the risk of primary open angle glaucoma, Graefes Arch. Clin. Exp. Ophthalmol. 255 (2017) 995–1001.

[44] Y. Nakano, et al., Toll-like receptor 4 inhibitor protects against retinal ganglion cell damage induced by optic nerve crush in mice, J. Pharmacol. Sci. 133 (2017) 176–183.

[45] E. Shibuya, et al., Association of Toll-like receptor 4 gene polymorphisms with normal tension glaucoma, Invest. Ophthalmol. Vis. Sci. 49 (2008) 4453–4457.

[46] Y. Hara, et al., Presynaptic mitochondrial morphology in monkey prefrontal cortex correlates with working memory and is improved with estrogen treatment, Proc. Natl. Acad. Sci. U. S. A. 111 (2014) 486–491.

[47] A.B. Noske, A.J. Costin, G.P. Morgan, B.J. Marsh, Expedited approaches to whole cell electron tomography and organelle mark-up in situ in high-pressure frozen pancreatic islets, J. Struct. Biol. 161 (2008) 298–313.

[48] G.B. John, et al., The mitochondrial inner membrane protein mitofilin controls cristae morphology, Mol. Biol. Cell 16 (2005) 1543–1554.

[49] A.E. Dikalova, et al., Sirt3 impairment and SOD2 hyperacetylation in vascular oxidative stress and hypertension, Circ. Res. 121 (2017) 564–574.

[50] X. Liu, et al., Sirt3-dependent deacetylation of SOD2 plays a protective role against oxidative stress in oocytes from diabetic mice, Cell Cycle 16 (2017) 1302–1308.

[51] C. Harada, et al., ASK1 deficiency attenuates neural cell death in GLAST-deficient mice, a model of normal tension glaucoma, Cell Death Differ. 17 (2010) 1751–1759.

[52] C. Wang, Y.L. Ren, J. Zhai, X.Y. Zhou, J. Wu, Down-regulated LAMA4 inhibits oxidative stress-induced apoptosis of retinal ganglion cells through the MAPK signaling pathway in rats with glaucoma, Cell Cycle 18 (2019) 932–948.

[53] Y. Chen, et al., Common variants near ABCA1 and in PMM2 are associated with primary open-angle glaucoma, Nat. Genet. 46 (2014) 1115–1119.

[54] P. Gharahkhani, et al., Common variants near ABCA1, AFAP1 and GMDS confer risk of primary open-angle glaucoma, Nat. Genet. 46 (2014) 1120–1125.

[55] P.G. Hysi, et al., Genome-wide analysis of multi-ancestry cohorts identifies new loci influencing intraocular pressure and susceptibility to glaucoma, Nat. Genet. 46 (2014) 1126–1130.

[56] Y. Jung, K. Han, H.Y.L. Park, S.H. Lee, C.K. Park, Metabolic Health, obesity, and the risk of developing open-angle glaucoma: metabolically healthy obese patients versus metabolically unhealthy but normal weight patients, Diabetes Metab. J (2019), https://doi.org/10.4093/dmj.2019.0048.

[57] J.H. Kang, et al., Association of statin use and high serum cholesterol levels with risk of primary open-angle glaucoma, JAMA Ophthalmol 137 (2019) 756–765.

[58] L. Li, et al., Reduced annexin A1 secretion by ABCA1 causes retinal inflammation and ganglion cell apoptosis in a murine glaucoma model, Front. Cell. Neurosci. 12 (2018) 347.

[59] A. Bringmann, P. Wiedemann, Muller glial cells in retinal disease, Ophthalmologica 227 (2012) 1–19.

[60] D. Morzaev, et al., Toll-like receptor-4 knockout mice are more resistant to optic nerve crush damage than wild-type mice, Clin. Exp. Ophthalmol. 43 (2015) 655–665.

[61] G. Dvoriantchikova, D.J. Barakat, E. Hernandez, V.I. Shestopalov, D. Ivanov, Toll-like receptor 4 contributes to retinal ischemia/reperfusion injury, Mol. Vis. 16 (2010) 1907–1912.

[62] R. Vohra, J.C. Tsai, M. Kolko, The role of inflammation in the pathogenesis of glaucoma, Surv. Ophthalmol. 58 (2013) 311–320.

[63] M. Kim, et al., Angiogenesis in glaucoma filtration surgery and neovascular glaucoma: A review, Surv. Ophthalmol. 60 (2015) 524–535.

[64] F. Schuettauf, et al., Retinal neurodegeneration in the DBA/2J mouse-a model for ocular hypertension, Acta Neuropathol. 107 (2004) 352–358.

[65] C. Luo, et al., Glaucomatous tissue stress and the regulation of immune response through glial Toll-like receptor signaling, Invest. Ophthalmol. Vis. Sci. 51 (2010) 5697–5707.

[66] D. Nguyen, et al., A new vicious cycle involving glutamate excitotoxicity, oxidative stress and mitochondrial dynamics, Cell Death Dis. 2 (2011) e240.

[67] M.S. Shim, et al., Mitochondrial pathogenic mechanism and degradation in optineurin E50K mutation-mediated retinal ganglion cell degeneration, Sci. Rep. 6 (2016) 33830.

[68] W.K. Ju, et al., Increased optic atrophy type 1 expression protects retinal ganglion cells in a mouse model of glaucoma, Mol. Vis. 16 (2010) 1331–1342.

[69] M.L. Risner, S. Pasini, M.L. Cooper, W.S. Lambert, D.J. Calkins, Axogenic mechanism enhances retinal ganglion cell excitability during early progression in glaucoma, Proc. Natl. Acad. Sci. U. S. A. 115 (2018) E2393–E2402.

[70] J.R. Tribble, et al., Midget retinal ganglion cell dendritic and mitochondrial degeneration is an early feature of human glaucoma, Brain Commun 1 (2019) fcz035.

[71] J. Yin, P. Han, Z. Tang, Q. Liu, J. Shi, Sirtuin 3 mediates neuroprotection of ketones against ischemic stroke, J. Cerebr. Blood Flow Metabol. 35 (2015) 1783–1789.

[72] A. Cheng, et al., Mitochondrial SIRT3 mediates adaptive responses of neurons to exercise and metabolic and excitatory challenges, Cell Metabol. 23 (2016) 128–142.

[73] X. Qiu, K. Brown, M.D. Hirschey, E. Verdin, D. Chen, Calorie restriction reduces oxidative stress by SIRT3-mediated SOD2 activation, Cell Metabol. 12 (2010) 662–667.

[74] Y. Chen, et al., Tumour suppressor SIRT3 deacetylates and activates manganese superoxide dismutase to scavenge ROS, EMBO Rep. 12 (2011) 534–541.

[75] Y. Chen, et al., Mesenchymal stem cells attenuate diabetic lung fibrosis via adjusting sirt3-mediated stress responses in rats, Oxid Med Cell Longev 2020 (2020) 8076105.

[76] A.E. Dikalova, et al., Mitochondrial deacetylase Sirt3 reduces vascular dysfunction and hypertension while Sirt3 depletion in essential hypertension is linked to vascular inflammation and oxidative stress, Circ. Res. 126 (2020) 439–452.

[77] Y. Imamura, et al., Drusen, choroidal neovascularization, and retinal pigment epithelium dysfunction in SOD1-deficient mice: A model of age-related macular degeneration, Proc. Natl. Acad. Sci. U. S. A. 103 (2006) 11282–11287.

[78] N. Ban, et al., Neuroprotective role of retinal SIRT3 against acute photo-stress, NPJ Aging Mech Dis 3 (2017) 19.

[79] J. Han, J.D. Lee, L. Bibbs, R.J. Ulevitch, A MAP kinase targeted by endotoxin and hyperosmolarity in mammalian cells, Science 265 (1994) 808–811.

[80] X. Cheng, C. Peuckert, S. Wolfl, Essential role of mitochondrial Stat 3 in p38 (MAPK) mediated apoptosis under oxidative stress, Sci. Rep. 7 (2017) 15388.

[81] Q. Yu, et al., Mitochondrial dysfunction triggers synaptic deficits via activation of p38 MAP kinase signaling in differentiated alzheimer's disease trans-mitochondrial cybrid cells, J Alzheimers Dis 59 (2017) 223–239.

[82] J. Chen, et al., Phosphorylation of Parkin at serine 131 by p38 MAPK promotes mitochondrial dysfunction and neuronal death in mutant A53T alpha-synuclein model of Parkinson's disease, Cell Death Dis. 9 (2018) 700.

[83] Y.J. Kang, et al., Macrophage deletion of p38alpha partially impairs lipopolysaccharide-induced cellular activation, J. Immunol. 180 (2008) 5075–5082.

[84] M. Otsuka, et al., Distinct effects of p38alpha deletion in myeloid lineage and gut epithelia in mouse models of inflammatory bowel disease, Gastroenterology 138 (2010) 1255–1265, 1265 e1251-1259.

[85] L. Huang, et al., Inhibitory effects of p38 inhibitor against mitochondrial dysfunction in the early brain injury after subarachnoid hemorrhage in mice, Brain Res. 1517 (2013) 133–140.

[86] A. Bohush, G. Niewiadomska, A. Filipek, Role of mitogen activated protein kinase signaling in Parkinson's disease, Int. J. Mol. Sci. 19 (2018).

[87] N. Sawe, G. Steinberg, H. Zhao, Dual roles of the MAPK/ERK1/2 cell signaling pathway after stroke, J. Neurosci. Res. 86 (2008) 1659–1669.

[88] X. Zhang, R. Zhang, J. Chen, J. Wu, Neuroprotective effects of DAAO are mediated via the ERK1/2 signaling pathway in a glaucomatous animal model, Exp. Eye Res. 190 (2020) 107892.

[89] Y. Zhou, V. Pernet, W.W. Hauswirth, A. Di Polo, Activation of the extracellular signal-regulated kinase 1/2 pathway by AAV gene transfer protects retinal ganglion cells in glaucoma, Mol. Ther. 12 (2005) 402–412.

[90] I.H. Pang, H. Zeng, D.L. Fleenor, A.F. Clark, Pigment epithelium-derived factor protects retinal ganglion cells, BMC Neurosci. 8 (2007) 11.

[91] M. Almasieh, C.J. Lieven, L.A. Levin, A. Di Polo, A cell-permeable phosphine-borane complex delays retinal ganglion cell death after axonal injury through activation of the pro-survival extracellular signal-regulated kinases 1/2 pathway, J. Neurochem. 118 (2011) 1075–1086.

[92] J. Wang, et al., Anatomy and spatial organization of Muller glia in mouse retina, J. Comp. Neurol. 525 (2017) 1759–1777.

[93] X. Wei, K.S. Cho, E.F. Thee, M.J. Jager, D.F. Chen, Neuroinflammation and microglia in glaucoma: time for a paradigm shift, J. Neurosci. Res. 97 (2019) 70–76.

[94] A. Bosco, et al., Neurodegeneration severity can be predicted from early microglia alterations monitored in vivo in a mouse model of chronic glaucoma, Dis Model Mech 8 (2015) 443–455.

[95] A.I. Ramirez, et al., The role of microglia in retinal neurodegeneration: Alzheimer's disease, Parkinson, and glaucoma, Front. Aging Neurosci. 9 (2017) 214.

[96] M. Wang, W. Ma, L. Zhao, R.N. Fariss, W.T. Wong, Adaptive Muller cell responses to microglial activation mediate neuroprotection and coordinate inflammation in the retina, J. Neuroinflammation 8 (2011) 173.